Master Thesis

Technische Universität Wien
Institute of Telecommunications

Influence of Fast Movement on DOA Algorithms for mmWave Channels

Daniel Schützenhöfer, B.Sc.
student number: 01129661

Supervision:
Univ. Prof. Dipl.-Ing. Dr.techn. Markus Rupp
Projektass. B.Sc. Dipl.-Ing. Dr.techn. Stefan Pratschner

Statement on Academic Integrity

I hereby declare and confirm with my signature that the master thesis is exclusively the result of my own autonomous work, based on my research and literature published, which is seen in the notes and bibliography used. I also declare that no part submitted has been made in an inappropriate way, whether by plagiarizing or infringing on any third person's copyright. Finally, I declare that no part submitted has been plagiarized for any other paper in another higher education institution, research institution or educational institution.

Vienna, May 2022

_____ _____
Author's signature   Supervisor's signature

Abstract

Virtual antenna arrays are employed on the roof of high-speed trains to sound the channel between a train and a fixed base station. Because high-speed trains are moving fast during such a measurement, high Doppler shifts are experienced. The laboratory setup proposed in this thesis allows repeatable measurements at the same antenna positions in standstill and at high speed and also ensures a fair comparison between classical sub $6\,\mathrm{GHz}$ frequencies and millimeter wave (mmWave) frequencies. In this work, I compare the performance of common direction of arrival (DOA) estimation algorithms such as the Bartlett beamformer or multiple signal classification (MUSIC) at different speeds and frequencies under the same conditions. I show that the estimated angular power spectrum changes drastically if the transmit antenna array is in motion during the measurement. At high speed, both algorithms show a high mean angular error. At high velocities, the angular error can amount to $\approx 40\%$. A simulation confirms that the Doppler effect in combination with the change of the antenna position causes an amplitude change of the estimated angular power spectrum. It also introduces an angular shift. The mean angular error in the simulation goes up to $\approx 11.5\%$ depending on the transmit frequency and velocity. The unique environment of the measurement could lead to a larger mean angular error. A reduction of the symbol duration in the simulation leads to a significantly lower angular mean error. The high errors indicate that the proposed DOA estimation algorithms are not consistent anymore at fast movement.

Kurzfassung

Virtuelle Antennengruppen werden auf dem Dach von Hochgeschwindigkeitszügen eingesetzt, um den drahtlosen Kanal zwischen einem Zug und einer festen Basisstation zu bestimmen. Da sich Hochgeschwindigkeitszüge während einer solchen Messung schnell bewegen, kommt es zu starken Dopplerverschiebungen. Der in dieser Arbeit vorgeschlagene Laboraufbau ermöglicht wiederholbare Messungen an denselben Antennenpositionen im Stillstand sowie bei hoher Geschwindigkeit und gewährleistet einen validen Vergleich zwischen klassischen Frequenzen unter 6 GHz und Millimeterwellenfrequenzen. In dieser Arbeit vergleiche ich das Verhalten gängiger Algorithmen zur Schätzung der Ankunftsrichtungen wie den Bartlett-Beamformer Algorithmus oder den Multiple Signal Classification (MUSIC) Algorithmus bei verschiedenen Geschwindigkeiten und Frequenzen unter denselben Bedingungen. Ich zeige, dass sich das geschätzte Winkelleistungsspektrum drastisch ändert, wenn sich die Sendeantennengruppe während der Messung bewegt. Bei hohen Geschwindigkeiten weisen beide Algorithmen einen hohen mittleren Winkelfehler auf. Bei hohen Geschwindigkeiten kann der Winkelfehler bis zu $\approx 40\%$ betragen. Eine Simulation bestätigt, dass der Dopplereffekt in Kombination mit der Änderung der Antennenposition eine Amplitudenänderung des geschätzten Winkelleistungsspektrums verursacht. Außerdem führt er zu einer Winkelverschiebung. Der mittlere Winkelfehler in der Simulation beträgt bis zu $\approx 11,5\%$ in Abhängigkeit von der Sendefrequenz und der Geschwindigkeit. Die besondere Umgebung der Messung könnte möglicherweise zu einem höheren mittleren Winkelfehler als in der Simulation führen. Eine Reduzierung der Symboldauer in der Simulation führt zu einem deutlich geringeren mittleren Winkelfehler. Der hohe Fehler zeigt, dass die vorgeschlagenen DOA-Schätzalgorithmen bei schnellen Bewegungen nicht mehr konsistent sind.

Table of Abbreviations

3G   Third Generation

4G   Fourth Generation

5G   Fifth Generation

AWG   Arbitrary Waveform Generator

CAZAC   constant amplitude zero autocorrelation

DOA   direction of arrival

FPGA   Field Programmable Gate Array

GB   gigabytes

IDFT   inverse diskrete fourier-transformation

IF   intermediate frequency

IFFT   Inverse Fast Fourier Transformation

IoT   Internet of Things

LO   local oscillator

MIMO   multiple-input multiple-output

mmWave   millimeter wave

MPC   multi-path components

MUSIC   multiple signal classification

MVAA   moving virtual antenna array

NLOS   non-line-of sight

OFDM   Orthogonal Frequency-Division Multiplexing

RF   radio frequency

SIMO   single input multiple output

SNR   Signal-to-noise ratio

URA	Uniform Rectangular Array
VAA	virtual antenna array
V2X	vehicle-to-everything

Contents

1 Introduction

1.1 Motivation

Data traffic in Fifth Generation (5G) or nowadays Sixth Generation wireless communication is rapidly growing. This trend will likely further increase over the next decade with the growing interest in video streaming, remote working and the rise of the Internet of Things (IoT). To meet the demand for high data rates, 5G communication move to technologies that operate at mmWave frequencies. The mmWave frequency band n258, which is a commonly used frequency band in 5G networks, uses a carrier frequency of 26GHz. Another positive effect that comes with mmWave frequencies in contrast to lower frequency bands is that they are less crowded.

A second approach to satisfy the high data rate of 5G is using multiple-input multiple-output (MIMO) and massive MIMO systems. With an increasing number of antennas, the hardware complexity gets high for MIMO channel measurements. Therefore, the method of virtual antenna array (VAA)s is employed [1, 2, 3, 4]. In the VAA approach the channel sounding is performed with only one antenna element. The antenna is mounted on a mechanical guide which enables the movement to different locations. The transmit antenna is sequentially re-positioned to the array positions forming an antenna array virtually in space. The channel sounding is done consecutively in time for each antenna position by transmitting the same channel sounding sequence. During the channel sounding procedure the antenna is in standstill, which means there is only motion in between the measurements. A measurement at a single antenna position can take anytime from seconds up to a few minutes. The re-positioning of the antenna between the measurements is also not infinitely fast and takes a significant amount of time. For a large array size this procedure can take several minutes up to hours of measurement time. This means that the environment and the measurement equipment on transmitter and receiver side have to be static during the whole measurement procedure [5]. Therefore, VAA measurements are often performed in indoor scenarios and during the night so the wireless channel is not biased by moving people or objects.

In [6], the authors introduce a VAA scheme for a high-speed railway scenario because there are several difficulties and constraints by implementing multiple antennas on top of high-speed trains. The channel sounding is performed via a single antenna mounted on top of the train. The same channel sounding sequence is repeated several times after a given repetition time. During the measurement, the train is moving with a constant speed of $350\,\mathrm{km/h}$. Due to the movement of the train, the antenna position is different for every channel sounding sequence. The movement of the train is similar to the re-positioning of the VAA approach. The adjacent samples of the measured

channel state information can be regarded as several antenna array elements. In contrast to a VAA, in the high-speed train scenario the antenna is also in motion during the channel sounding process. This special case of a VAA where the antenna is in constant movement is referred to as a moving virtual antenna array (MVAA). The MVAA measurements are then used for spacial characterization [7, 8, 9].

One problem in performing MVAA measurements in a high-speed railway scenario is the repeatability of the measurement. Measuring several times at different velocities is very time-consuming and impractical. Furthermore, it is very hard to measure at the exact same antenna positions. There is also a problem for conducting comparable multi-band measurements involving sub $6\,\mathrm{GHz}$ and mmWave frequencies. The two antennas for the different frequency bands cannot be placed at the same position at the same time. There are two possible solutions to address this issue. First, measuring with each antenna at the exact same position but at different times. Second, measuring at the exact same time with the two different antennas positioned some centimeters apart on the roof of the train. This allows you to measure at the same time, but the offset of several wavelengths can result in a different small scale fading behavior. With the special measuring setup using the Rotary Unit of the TU Wien, I am able to do repeatable high-speed measurements with the same indoor environment at different frequencies at the exact same antenna position.

Two well-known and frequently used algorithms for DOA estimation are the Bartlett beamformer and the MUSIC algorithm. They are often applied because of their straightforward implementation. Both algorithms are implemented for a wide range of applications, including scenarios where the transmit or receive antenna is in motion [10, 11, 12, 13]. The movement of either the transmit antenna, the receive antenna, or the objects leads to a frequency shift, also known as the Doppler shift. Neither the Bartlett beamformer nor the MUSIC algorithm takes this frequency shift into account. Doppler shifts are usually relatively small because the velocity is always marginal in comparison to the speed of light. Since the Doppler shifts are so small, it makes sense to ask whether they have an impact on DOA estimations.

The size of the Doppler shift is not only depending on the movement speed of the antennas. It also depends on the applied transmit frequency. As mentioned before, the trend in wireless communication is towards using mmWave frequencies. An increase of a factor of ten in frequency would also lead to a tenfold higher Doppler frequency shift. This increase of the Doppler shift for mmWave could lead to a higher estimation error for DOA estimations, especially for algorithms like the Bartlett Beamformer or the MUSIC algorithm, which do not consider the Doppler effect.

With the measuring setup proposed in this thesis, I am able to make repeatable VAA and MVAA measurements at different velocities in the exact same indoor environment. Furthermore, the setup allows for comparison of measurements at sub $6\,\mathrm{GHz}$ frequencies with measurements at mmWave frequency. This enables me to evaluate the influence of fast movement on frequently applied DOA estimation algorithms at different frequencies.

1.2 Contribution and Outline

In this work, I investigate the influence of movement on frequently used DOA estimation algorithms, namely the Bartlett beamformer and the MUSIC algorithm. The evaluation is done in two different ways: First with the help of measurements and second with a simulation.

First, I show the influence with the help of measurements as described in Section 2. I perform a VAA measurement and two MVAA measurements at $20\,\mathrm{km/h}$ and $200\,\mathrm{km/h}$. Further, the whole measurement is done at two different transmit frequencies of $2.55\,\mathrm{GHz}$ and $25.5\,\mathrm{GHz}$, which allows to determine the impact of the higher Doppler shift at mmWave frequencies. Details of the performed measurement campaign are discussed in Section 2.1. The measurement setup allowing repeatable indoor measurements at standstill and at high speed is presented in Section 2.2. Furthermore I show the most important parameters used in the measurement. The channel sounding procedure is described in Section 2.3. The resulting channel state information is used for DOA estimation in Section 2.4. To estimate the DOAs, I choose two different well known and frequently used algorithms. Firstly, I employ the conventional beamformer, which is also called the Bartlett beamformer. The important aspects of the algorithm are described in Section 2.4.1. Secondly, I apply a subspace-based DOA estimation method, the MUSIC algorithm, which is shortly described in Section 2.4.2.

The results of the measurements are discussed in Section 2.5. I show that the estimated angular power spectrum changes drastically if the transmit antenna is in motion during the VAA measurement. To evaluate the error of the estimated DOAs, I introduce the circular variance and the angular mean in Section 2.5.3. For most of the scenarios, the error of the angular mean is very high.

To verify the influence of the Doppler effect on the two presented DOA estimation methods, I create a simulation proposed in Section 3. The simulation scenario, which should be as close to the measurement scenario as possible, is described in Section 3.1. For the standstill scenario where the antenna array is not moving, I introduce a time-invariant channel model in Section 3.2. The movement of the antenna leads to a shift of the received frequency (Doppler shift). By taking the Doppler effect

into account, the channel gets time-variant. The time-variant channel model, which represents the MVAA scenario is introduced in Section 3.3. Until now, the antenna motion during one symbol duration has been neglected because the covered distance during one symbol or snapshot is relatively small in comparison to the distance between transmitter and receiver. In Section 3.4, this antenna motion is added to the time-variant channel model. Further simulation results are shown in Section 3.5. In Section 3.6, I discuss and compare the simulation and the measurement.

1.3   Notation

I denote vectors by lowercase boldface letters, such as $\mathbf{x}$, and matrices by uppercase boldface letters, such as $\mathbf{X}$. Further, I denote the entry from the n-th row and the k-th column of matrix $\mathbf{X}$ by $X_{n,k}$. I denote the Frobenius norm by $\|\cdot\|$ and the absolute value of a scalar as well as the cardinality of a set by $|\cdot|$. The operator $(\cdot)^{\mathsf{T}}$ denotes the transpose of a vector or matrix and the operator $(\cdot)^{\mathsf{H}}$ denotes the conjugate transpose of a vector or matrix. The operator $\otimes$ denotes the Kronecker product.

2   Channel Measurement

I perform wireless channel measurements in an indoor environment at the campus of the TU Wien. I introduce the measurement campaign and all six different scenarios in Section 2.1. The special measurement setup introduced in Section 2.2 allows repeatable measurements at different velocities at a transmit frequency of $2.55\,\mathrm{GHz}$ and $25.5\,\mathrm{GHz}$. In Section 2.3, I explain details of the channel estimation process. The channel estimates are then used for DOA estimation. I implemented two very common DOA estimation methods the Bartlett beamformer and the MUSIC algorithm. I introduce these algorithms in Section 2.4. The results of the DOA estimation conducting a VAA MVAAand a are presented in Section 2.5. First, I analyze the angular power spectrum for the standstill scenario and second, the scenarios where the transmit antenna is in motion. Further, I introduce the metric of angular mean and circular variance in Section 2.5.3. This enables a mathematical way to evaluate the error introduced by the antenna motion in the MVAA scenarios.

2.1   Measurement Campaign

I performed wireless channel measurements in six different scenarios at the campus of the TU Wien, Austria. These scenarios varied in velocity and frequency: three of them were conducted at a frequency of $2.55\,\mathrm{GHz}$ and velocities of $0\,\mathrm{km/h}$, $20\,\mathrm{km/h}$ and $200\,\mathrm{km/h}$. I apply the same velocities for the other three scenarios, which were conducted at a center frequency of $25.5\,\mathrm{GHz}$. The transmit frequency of $2.55\,\mathrm{GHz}$ corresponds to a free space wavelength of $\lambda \approx 118\,\mathrm{mm}$ and the frequency of $25.5\,\mathrm{GHz}$ correspond to a free space wavelength of $\lambda \approx 11.8\,\mathrm{mm}$. The transmitter and the receiver are both located in an office environment. With the help of the rotary unit, which will be introduced in the following chapter, the transmit antenna is moved on a circular arc around a central pivot with a constant velocity. The receiving antenna is static on a laboratory table in the neighboring room. The distance from the transmit antenna array to the receive antenna is $R \approx 7.5\,\mathrm{m}$. The corresponding floor plan and the location of the antennas are shown in Fig. 1.

Since the rotary unit contains only one transmit antenna, I employ the method of generating an antenna array virtually. This measurement technique performs channel sounding with a single antenna instead of an N-size antenna array. The single antenna is repositioned to all N different positions. The antenna array is then assembled virtually in the post-processing. A condition for creating a VAA is the environment being stationary during the whole measurement procedure. In other words, the channel must be time-invariant between the measurements because the relocation of the antenna takes a significant amount of time. Therefore, the measurement campaign is performed during the night so that moving people or objects can not influence
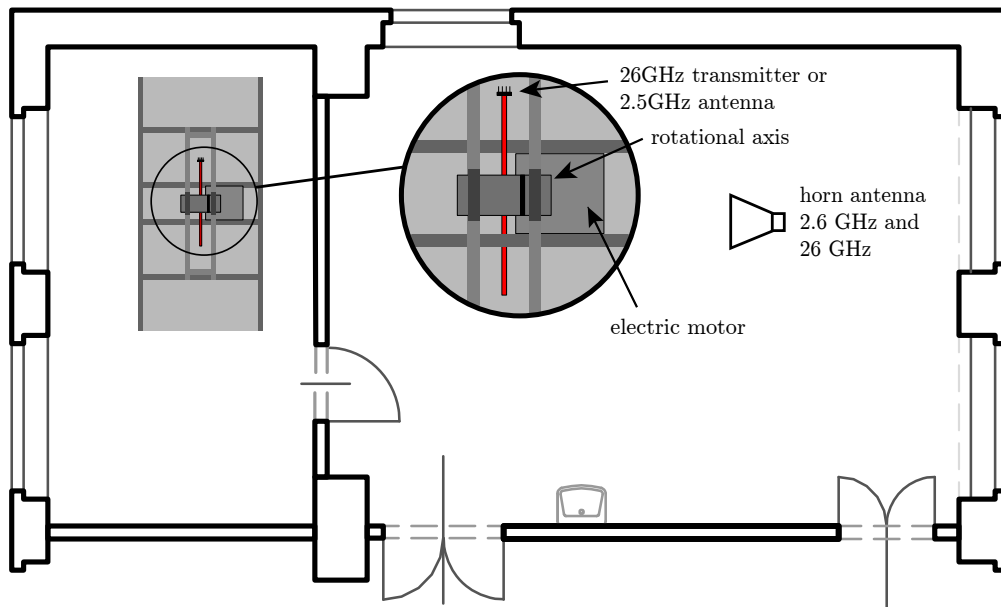
Figure 1: Measurement environment. The transmit antenna is mounted on the rotary unit on the left. The receiving antenna is located in the other room. They are approximately 7.5 meters apart.

the measurement. In VAA measurements, the antenna is only moving in between the measurements. Authors of [6] introduce a new method by conducting a VAA measurement employing a single transmit antenna on the top of a high-speed train. The train is moving with a constant velocity of $350\,\mathrm{km/h}$. Several sounding sequences are sent over the same antenna after pre-defined time intervals. The adjacent time samples of the measured channel state information can be regarded as several antenna array elements. The samples of the channel estimation at different time stamps form a VAA. In contrast to the usual VAA approach, the antenna on the train is in constant movement during the sounding procedure. This special case of a VAA where the antenna is in constant movement during the measurement is referred to as a MVAA.

In this measurement campaign, both a VAA for the standstill scenario and a MVAA for the motion scenarios at $20\,\mathrm{km/h}$ and $200\,\mathrm{km/h}$ are employed. For simplicity reason, I will refer to both as VAA in the following chapters. In the standstill scenario, the transmit antenna is fixed at the top position. In the motion scenarios, the transmit antenna travels a certain distance d. This distance is dependent on the symbol duration T_S, the number of symbols per snapshot and the velocity v. A more detailed discussion of the chosen parameters are given in Section 2.2.3.

For all six scenarios, I measured 144 different transmit antenna positions. I then form a

Uniform Rectangular Array (URA) with an antenna spacing of 0.4λ. The URA consists of $N_x = 18$ antenna in the x-direction and $N_y = 8$ in the y-direction. After channel estimation, the resulting channel coefficients of the measurement are used for a DOA estimation, which is covered in Section 2.4.

2.2   Measurement Setup

On the transmitter side, I utilize the Rotary Unit of the TU Wien [14, 15, 16]. This allows repeatable indoor to indoor and indoor to outdoor measurements at different velocities and transmit frequencies. The mechanical setup of the rotary unit is shown in Fig. 2. Two different transmit antennas with a center frequency of $2.55\,\mathrm{GHz}$, or $25.5\,\mathrm{GHz}$, can be placed on top of an $1\,\mathrm{m}$ long rotary arm. A frequency-controlled asynchronous motor enables the rotation of the arm with a velocity up to $500\,\mathrm{km/h}$. The transmit antenna moves on a circle around a central pivot. The whole rotary unit is placed on a sliding board, which can be moved by 81 centimeter along the x-axis and by 33 centimeter along the y-axis.

To produce repeatable measurements, it is important that the signal must be transmitted at the exact same arm position throughout the experiments. Therefore I build a device called the Trigger Unit. The Trigger Unit generates a trigger signal at any pre-defined angular position of the rotary arm within the circle. A magnetic ring decoder at the rotational axis delivers two phase shifted signals with 960 pulses per rotation and a reference signal, which occurs only once per rotation. The signals are then utilized by a quadrature encoder by a Field Programmable Gate Array (FPGA). This allows to resolve 960 different positions per rotation, which equals a position every $0.375°$ around the circle. If the rotary arm reaches the pre-defined position, a $100\,\mathrm{\mu s}$ long rectangular signal is delivered. In all measurement scenarios, the trigger unit provides a signal the moment the rotary arm reaches the top position (the rotary arm faces the ceiling). This guarantees that the measurement process starts at the same antenna position in each scenario.

2.2.1   Sub 6 GHz

In Fig. 3, the block diagram of the sub $6\,\mathrm{GHz}$ measurements is shown. The transmit signal is generated by an Arbitrary Waveform Generator (AWG) at a center frequency of $2.55\,\mathrm{GHz}$. After two amplifier stages, the signal is fed through a rotary joint to a monopole antenna, which is placed at the end of the rotary arm. On the receiver side, I employ a vertical dipole antenna. The received signal is then sampled by a signal analyzer (Rhode & Schwarz FSW67).
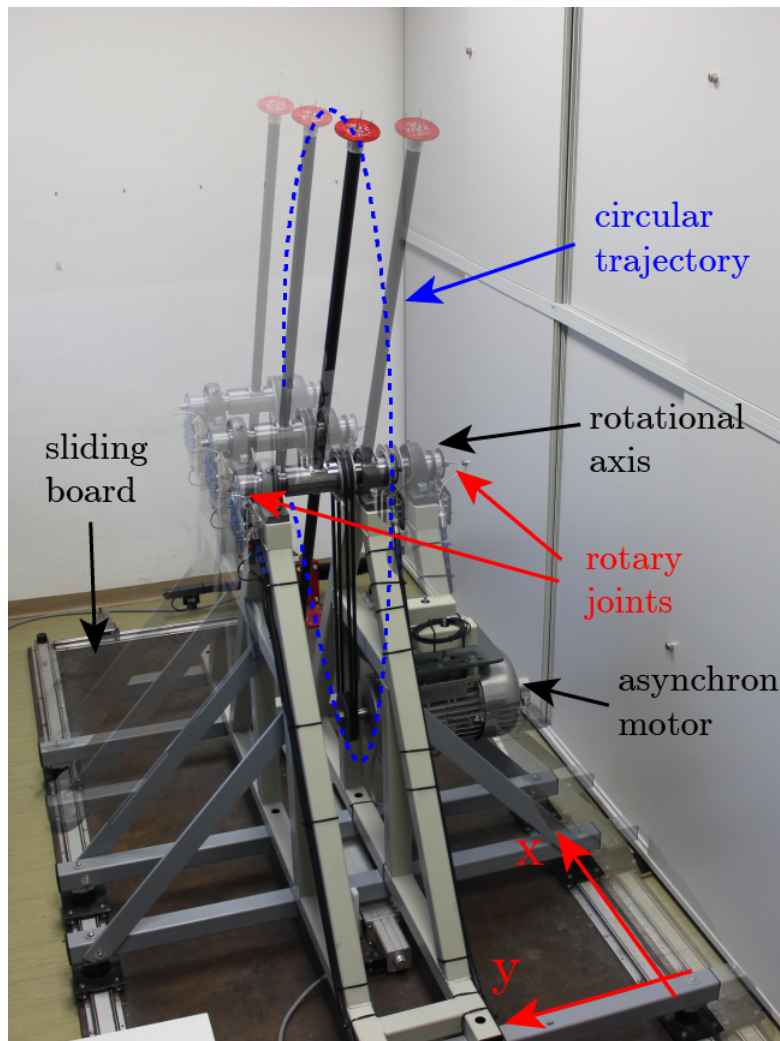
Figure 2: Rotary unit used to measure with the VAA and the MVAA. The whole setup can be moved in the x and the y direction.

To allow synchronization of transmitter and receiver side, the system needs a reference clock. This can be assured by a clock via a common oscillator, which is distributed via coaxial cable to all measurement devices. As a reference clock, I utilize the internal $100\,\mathrm{MHz}$ clock from the signal analyzer at the receiver.

2.2.2   Millimeter Wave

The measurement setup in the mmWave case is slightly different. Figure 4 shows the adjusted block diagram of the sub mmWave measurement. A mmWave transmitter [17] replaces the monopole antenna of the sub $6\,\mathrm{GHz}$ measurement. Because of the
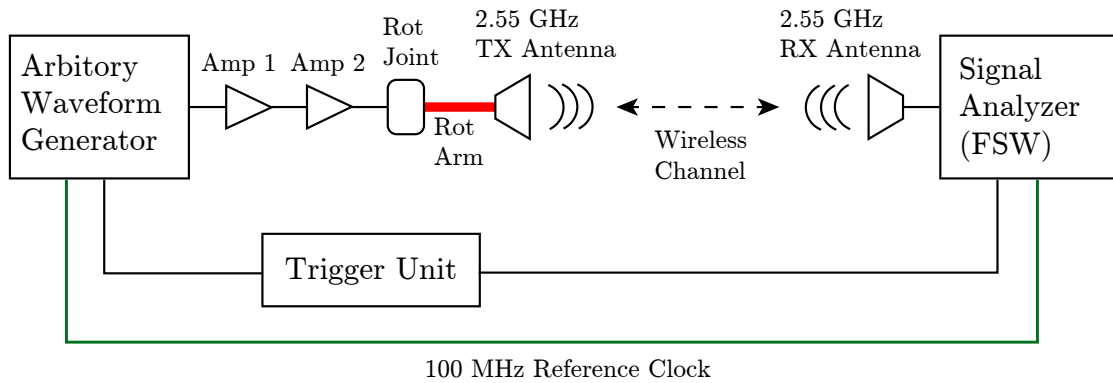
Figure 3: Block diagram of the measurement setup for the $2.55\,\text{GHz}$ scenarios.

mechanical properties of the rotary joint, which only supports signals with a frequency up to $12.4\,\text{GHz}$, a frequency up-conversion on the PCB of the mmWave transmitter is needed. To realize an up-conversion, two rotary joints are employed. One rotary joint is utilized for the intermediate frequency (IF) signal and the other for the local oscillator (LO) signal. The up-converter of the mmWave transmitter performs internal LO frequency doubling, which leads to a radio frequency (RF) frequency of

$$f_{RF} = 2f_{LO} + f_{IF}. \tag{1}$$

An LO frequency of $10\,\text{GHz}$ and an IF frequency of $5.5\,\text{GHz}$ results in the desired RF frequency of $25.5\,\text{GHz}$. The IF signal is generated by the AWG and the LO signal is generated by a continuous wave signal generator. Because of the higher frequency of mmWaves, a higher free space path loss must be overcome. Therefore, I employed a horn antenna with $15\,\text{dBi}$ gain as a receive antenna. The horn antenna has an half power beam width of $30°$. This is not optimal for DOA estimation because there is no $360°$ coverage and not all paths can be captured. To reduce the impact of the horn antenna on angular coverage of the captured paths, the receive antenna is placed near the wall facing the transmitter (see Fig. 1). Further, I assume that the waves reflected on the wall behind the receive antenna have a significant smaller impact. With this setup, it is possible to capture most of the dominant paths.
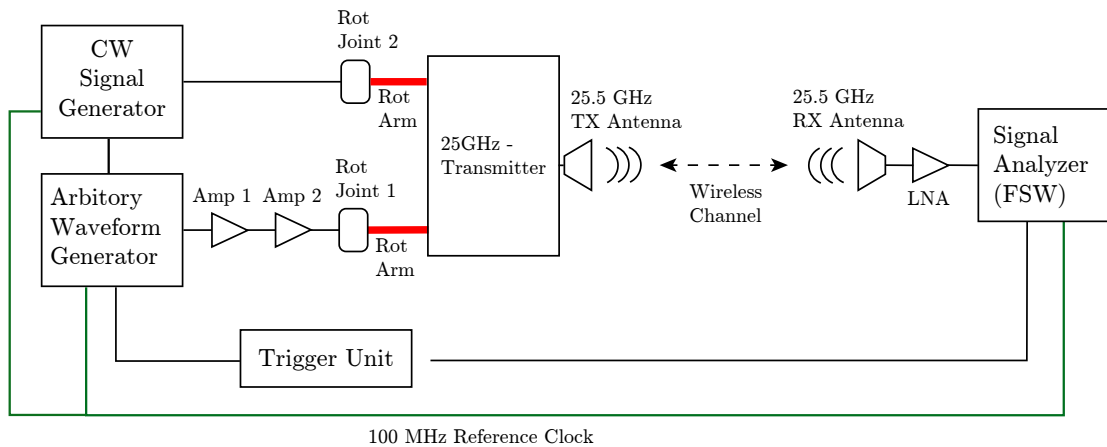
Figure 4: Block diagram of the measurement setup for the $25.5\,\mathrm{GHz}$ scenarios.

2.2.3 Measurement Parameter

The parameters are slightly different for each scenario. The bandwidth B of the signal depends on the $3\,\mathrm{dB}$ bandwidth of the corresponding antennas. The $2.55\,\mathrm{GHz}$ antenna supports a bandwidth of $B = 200\,\mathrm{MHz}$ and the $25.5\,\mathrm{GHz}$ antenna supports $500\,\mathrm{MHz}$.

In each measurement, I send 101 identical Orthogonal Frequency-Division Multiplexing (OFDM) symbols over the wireless channel. The first symbol is discarded at the receiver as a cyclic prefix. The remaining 100 symbols are referred to as one snapshot. Each symbol has a duration of T_{symb}. This leads to a snapshot duration of $T_{snap} = 100 T_{symb}$. The channel sounding procedure is further described in the next section.

In the motion scenarios, the antenna is moving with different velocities v. The traveled distance of the antenna during one measurement can then be calculated with $d = v T_{snap}$. For reasons of comparability of the given measurements, the traveled distance covered by the rotary arm should stay the same irrespective of the velocity. Depending on the scenario, the symbol duration T_{symb} is adjusted in a way that the distance is constant. For example, in Scenario A and Scenario C, the antenna is moving with a velocity of $20\,\mathrm{km/h}$. By choosing a symbol duration of $5\,\mu s$, the antenna moves a distance of $d = 100 T_{symb} v \approx 2.78\,\mathrm{mm}$. To cover the same distance $d = 2.78\,\mathrm{mm}$ in Scenario B and Scenario D, where the antenna is moving with $v = 200\,\mathrm{km/h}$, the symbol duration is adjusted by $T_{symb} = {}^{d}/_{100v} = 0.5\,\mu s$. The subcarrier spacing $F = {}^{1}/_{T_{symb}}$ and the number of subcarriers $N_{sub} = {}^{B}/_{F}$ are then calculated depending on the bandwidth B and the symbol duration T_{symb} of the

corresponding measurement scenario.

The rotary arm movement of $2.78\,\mathrm{mm}$ around the circle during the motion measurements corresponds to an angular change of $0.159°$. Because these angular changes are actually so minimal, I consider this -by definition circular- movement as a linear one.

All parameters for the different scenarios are summarized in Fig. 5.

	Velocity		
	20 km/h	200 km/h	standstill
Center Frequency — 2.55 GHz	subcarrier spacing = 200 kHz bandwidth = 200 MHz symbol duration = 5 µs meas. duration = 4 ms max. Doppler shift = 47 Hz symb/snap = 100 dist./snap. = 2.78mm n_{Sub} = 1000 **A**	subcarrier spacing = 2 MHz bandwidth = 200 MHz symbol duration = 0.5 µs meas. duration = 0.4 ms max. Doppler shift = 472 Hz symb/snap = 100 dist./snap. = 2.78mm n_{Sub} = 100 **B**	subcarrier spacing = 200 kHz bandwidth = 200 MHz symbol duration = 5 µs meas. duration = 4 ms symb/snap = 100 n_{Sub} = 1000 **E**
Center Frequency — 25.5 GHz	subcarrier spacing = 200 kHz bandwidth = 500 MHz symbol duration = 5 µs meas. duration = 4 ms max. Doppler shift = 472 Hz symb/snap = 100 dist./snap. = 2.78mm n_{Sub} = 2500 **C**	subcarrier spacing = 2 MHz bandwidth = 500 MHz symbol duration = 0.5 µs meas. duration = 0.4 ms max. Doppler shift = 4725 Hz symb/snap = 100 dist./snap. = 2.78mm n_{Sub} = 250 **D**	subcarrier spacing = 200 kHz bandwidth = 500 MHz symbol duration = 5 µs meas. duration = 4 ms symb/snap = 100 n_{Sub} = 2500 **F**

Figure 5: List of all parameters for the different scenarios

2.3 Channel Estimation

Wireless communication performance depends significantly on the propagation environment [18]. Reflection and refraction at different scattering objects create multiple paths between transmitter and receiver, which cause the same signal to be received at different times, with different phases and signal strength. To evaluate the characteristics of the measured wireless channel, I perform channel sounding. For channel sounding, I transmit an a priori known OFDM signal with different subcarrier spacings F, depending on the measurement scenario. The chosen subcarrier spacing for the different measurement scenarios are discussed in Section 2.2.3.

The transmit signal is a Zadoff-Chu sequence described in [19]. Zadoff-chu sequences are constant amplitude zero autocorrelation (CAZAC) sequences, which lead to a

frequency flat transmit spectrum. Zadoff-Chu sequences are employed in different fields because of their perfect periodic autocorrelation properties [20]. The u root Zadoff-Chu sequence at subcarrier position k is defined by [19]

$$x_u(k) = \begin{cases} \exp(-j\frac{\pi u k(n+1)}{N_{sub}}) & \text{for odd u} \\ \\ \exp(-j\frac{\pi u k^2}{N_{sub}}) & \text{for even u} \end{cases}, \tag{2}$$

where N_{sub} is the length of the Zadoff-Chu sequence, which in our case is equal to the number of subcarriers and u is the root index with $0 < u \leq N_{sub} - 1$. For simplicity, a root index of $u = 1$ is chosen. The OFDM symbol at time index m can be calculated by an inverse diskrete fourier-transformation (IDFT) of $x[k]$ with

$$x[m] = \frac{1}{N_{sub}} \sum_{k=0}^{N_{sub}-1} x[k] \exp\left(2\pi j \frac{nm}{N_{sub}}\right) = \text{IDFT}_{k \to m}\{x[k]\}. \tag{3}$$

I sent 101 repetitions of the same OFDM symbol over the wireless channel as a sounding sequence. The first of these 101 identical OFDM symbols is discarded at the receiver as a cyclic prefix. The remaining 100 symbols are referred as one snapshot. Averaging over the 100 received symbol of one snapshot results in a Signal-to-noise ratio (SNR) gain of $20\,\text{dB}$, which is important because of the lower SNR in the $25.5\,\text{GHz}$ measurement. This is only legit when the measured channel is time-independent for one snapshot duration.

The coherence time is the time duration over which the channel impulse response is not varying. It can be calculated with [21]

$$T_c = \frac{1}{2\nu_{max}}, \tag{4}$$

where ν_{max} is the maximum Doppler shift. The maximum Doppler shift is dependent on the transmit frequency and the velocity and is given by

$$\nu_{max} = f_c \frac{v}{c}, \tag{5}$$

where c is the speed of light. I assume that over one snapshot duration the wireless channel is being time-invariant because the snapshot duration is smaller than the coherence time for every measurement scenario in motion ($T_{snap} \leq T_c$). For example in Scenario D ($f_c = 25.5\,\text{GHz}, v = 200\,\text{km/h}$) the maximum Doppler shift is $\nu_{max} = 4.725\,\text{kHz}$, which leads to a coherence time of $T_c = 105.8\,\text{µs}$. The snapshot duration for Scenario D is $T_{snap} = 50\,\text{µs} \leq T_c$. The coherence time and snapshot time

of all scenarios are listed in Tab. 1.

	f_c [GHz]	v [km/h]	T_c [µs]	T_{snap} [µs]
Scenario A	2.5	20	10582.0	500
Scenario B	2.5	200	1058.2	50
Scenario C	25	20	1058.2	500
Scenario D	25	200	105.8	50

Table 1: The table summarizes the coherence time and snapshot time for all scenarios. It is shown that the coherence time is shorter than the snapshot duration for each measurement scenario. Therefore, the channel is considered to be time-independent for a snapshot duration.

The channel vector of a single input multiple output (SIMO) system with a rectangular antenna array of size N in the frequency domain is defined as

$$\mathbf{h}[k] = \begin{bmatrix} h_{1,1}[k] \\ h_{2,1}[k] \\ \vdots \\ h_{\mathsf{Nx},1}[k] \\ h_{1,2}[k] \\ \vdots \\ h_{\mathsf{Nx},2}[k] \\ \vdots \\ h_{\mathsf{Nx},\mathsf{Ny}}[k] \end{bmatrix}, \tag{6}$$

where the first index of $h_{n,m}$ is the n-th antenna element on the x-axis and the second index indicates the m-th antenna element on the y-axis.

The received signal vector for a N-element rectangular antenna array $\mathbf{y}[k] = \begin{bmatrix} y_1 & y_2 & \cdots & y_N \end{bmatrix}^{\mathsf{T}}$ can be written as

$$\mathbf{y}[k] = \mathbf{h}[k]x[k] + \mathbf{n}[k] \tag{7}$$

The same sounding sequence $x[k]$ given by (2) is used for every received antenna position and thus can be written as a scalar. The noise vector for each antenna element is represented by $\mathbf{n}[k]$.

To minimize the influence of the measurement equipment, I conducted a back to back calibration measurement for each measurement. The wireless channel is then estimated through least squares estimation with

$$\hat{\mathbf{h}}[k] = \frac{\mathbf{y}[k]}{x[k]}. \tag{8}$$
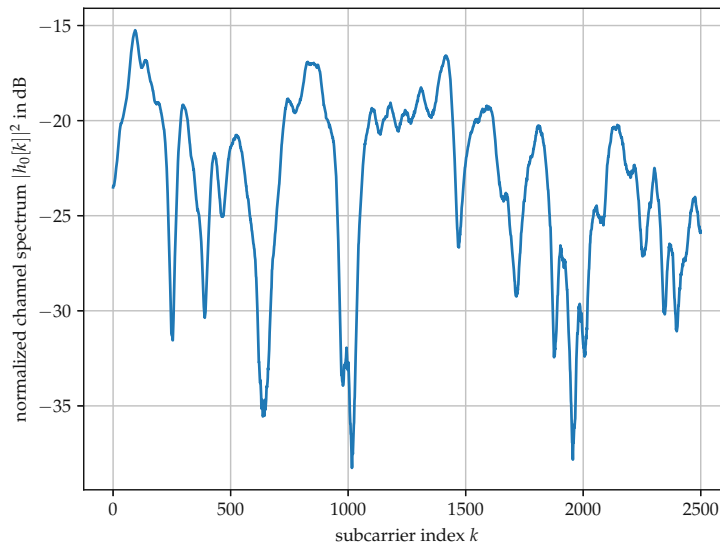
Figure 6 shows the measured frequency spectrum of the channel between the transmit antenna and one of the receive antennas $|h_{0,0}[k]|^2$ at each subcarrier index k of Scenario F ($f_c = 25.5\,\mathrm{GHz}$). The channel transfer function $h_{0,0}[k]$ shows multiple peaks and notches, which is typical for rich scattering environments. Performing an Inverse Fast Fourier Transformation (IFFT) on $h_{0,0}[k]$ results in an estimation of the channel impulse response, which is depicted in Fig. 7. The impulse response also shows typical multi-path propagation properties. The main propagation paths occuring at a delay smaller than $180\,\mathrm{ns}$.

Figure 6: Measured frequency spectrum of the channel between the transmit antenna and one receive antenna $|h_0[k]|^2$ at each subcarrier index k.
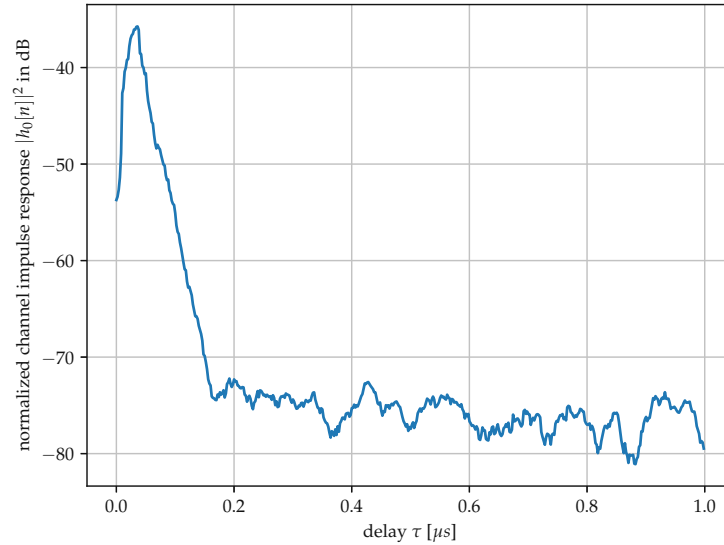
Figure 7: Impulse response of the channel between the transmit antenna and one receive antenna $|h_{0,0}[n]|^2$.

2.4   Direction of Arrival (DOA) Estimation

With a uniform linear array, the DOA estimate is ambiguous. To get a $360°$ coverage and to get rid of mirror images for azimuth angles, I employ a virtual URA. This is a planar array with a uniform rectangular grid and rectangular boundary. I chose N $=$ 144 different sampling points in the spatial domain with a uniform antenna spacing of $d = 0.4\lambda$. There are $N_x = 18$ antennas in the x-direction and $N_y = 8$ in the y-direction. The created antenna array in the measurement environment is shown in Fig. 8(a) and the antenna constellation in Fig. 8(b). For an N-element antenna array with P distinct DOAs, the output signal vector is written as

$$\underbrace{\begin{bmatrix} y_1[k] \\ y_2[k] \\ \vdots \\ y_N[k] \end{bmatrix}}_{\mathbf{y}[k]} = \underbrace{\begin{bmatrix} \mathbf{a}[\varphi_1, \theta_1] & \mathbf{a}[\varphi_2, \theta_2] & \dots & \mathbf{a}[\varphi_P, \theta_P] \end{bmatrix}}_{\mathbf{A}_{\varphi,\theta}} \underbrace{\begin{bmatrix} G[\varphi_1, \theta_1, k] \\ G[\varphi_2, \theta_2, k] \\ \vdots \\ G[\varphi_P, \theta_P, k] \end{bmatrix}}_{\mathbf{G}[\varphi,\theta,k]} x[k] + \mathbf{n}[k]. \qquad (9)$$

Here, the angle φ_p describes the azimuth angle of the p-th DOA and θ_p the elevation angle of the p-th DOA. The vector $\mathbf{y}[k]$ describes the noisy received signal at each

16

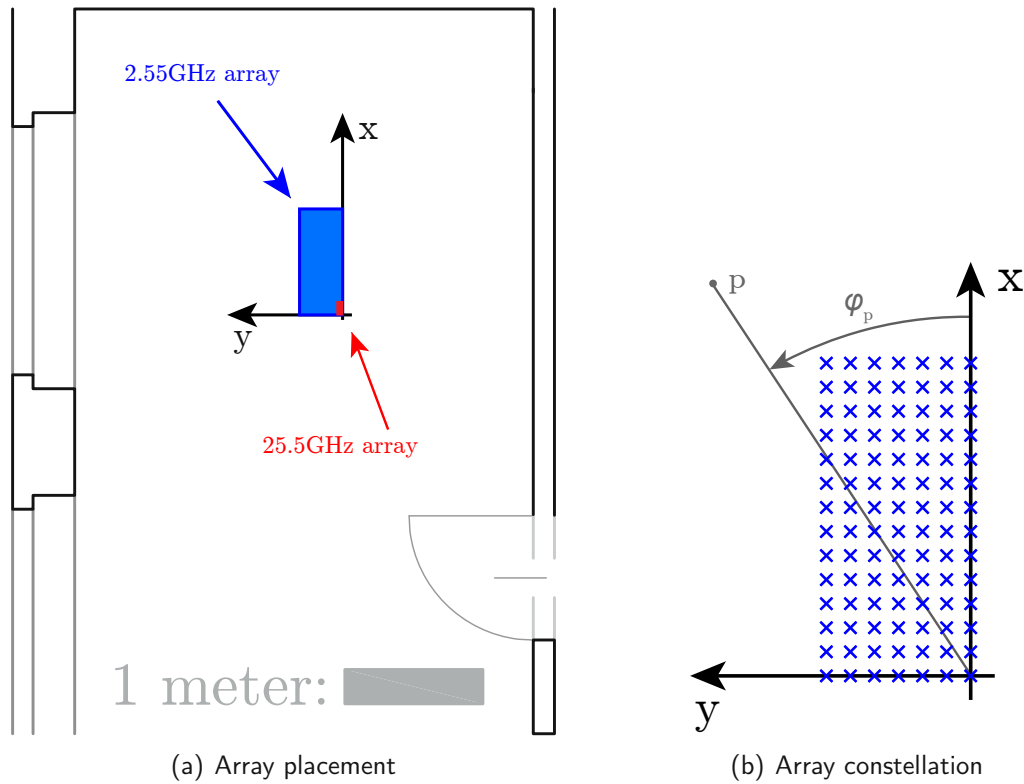(a) Array placement (b) Array constellation

Figure 8: Constellation of the virtual URA and the exact antenna placement in the office environment

antenna element $n = 1 \ldots N$ in the frequency domain where k is the subcarrier index. The angular amplitude spectrum is defined by the vector $\boldsymbol{G}[\varphi, \theta, k]$. Each vector entry represents the signal strength coming from direction φ_p at a given subcarrier with index k. The transmit signal in the frequency domain is given by $x[k]$ and the noise vector for each antenna element is represented by $\mathbf{n}[k]$. The steering vector is denoted by $\mathbf{a}[\varphi_p, \theta_p]$. A steering vector represents a set of phase delays accomplished by a plane wave when it reaches different antennas [22].

The steering vector $\mathbf{a}[\varphi, \theta]$ of a uniform rectangular array is expressed as [23]

$$\mathbf{a}[\varphi, \theta] = \mathbf{a}_\mathsf{y}[\varphi, \theta] \otimes \mathbf{a}_\mathsf{x}[\varphi, \theta] \tag{10}$$

where $\otimes$ denotes the Kronecker product, $\mathbf{a}_\mathsf{x}[\varphi, \theta]$ is the steering vector in the x-direction and $\mathbf{a}_\mathsf{y}[\varphi, \theta]$ is the steering vector in the y-direction.

The steering vectors $\mathbf{a}_x[\varphi, \theta]$ and $\mathbf{a}_y[\varphi, \theta]$ take on the form [24]

$$\mathbf{a}_x(\varphi, \theta) = \begin{bmatrix} 1 & e^{j\Psi_x} & \ldots & e^{j(N-1)\Psi_x} \end{bmatrix}^{\mathsf{T}} \tag{11}$$

$$\mathbf{a}_y(\varphi, \theta) = \begin{bmatrix} 1 & e^{j\Psi_y} & \ldots & e^{j(M-1)\Psi_y} \end{bmatrix}^{\mathsf{T}} \tag{12}$$

where Ψ_x and Ψ_y are defined as

$$\Psi_x = \frac{\omega}{c} d \cos(\varphi)\cos(\theta), \tag{13}$$

$$\Psi_y = \frac{\omega}{c} d \sin(\varphi)\cos(\theta) . \tag{14}$$

Here, ω denotes the angular frequency and c indicates the speed of light. Since TX and RX are approximately at the same height above the laboratory floor, we expect the dominant paths to occur at an elevation angle of $90°$. Next, the formulas above are simplified and the elevation angle dependency can be dropped. To estimate the DOAs, I chose two different well known and frequently used algorithms. Firstly, I employ the conventional beamformer, which is also called the Bartlett beamformer and secondly, a DOA estimation based on the MUSIC algorithm. As I mentioned, both of the algorithms are well-known in the field of DOA estimations and fairly popular. For reasons of readability and completeness, I will shortly introduce the important aspects of the algorithms in the following chapters.

2.4.1   Bartlett Beamformer or Conventional Beamformer

The Bartlett beamformer or conventional beamformer is a beamscan algorithm. The beamscan algorithm forms a conventional beam, scans it over the desired region and plots the magnitude squared of the output. The channel vector $\mathbf{h}[k]$ already described in (6) can also be written in matrix form

$$\mathbf{H} = \begin{bmatrix} \mathbf{h}[0] & \mathbf{h}[1] & \ldots & \mathbf{h}[K] \end{bmatrix} = \begin{bmatrix} h_{0,0}[0] & h_{0,0}[1] & \ldots & h_{0,0}[N_{sub-1}] \\ h_{1,0}[0] & h_{1,0}[1] & \ldots & h_{1,0}[N_{sub-1}] \\ \vdots & \vdots & \ddots & \vdots \\ h_{N_x,N_y}[0] & \ldots & \ldots & h_{N_x,N_y}[N_{sub-1}] \end{bmatrix} . \tag{15}$$

Here, the columns represent the N_{Sub} different subcarriers and the rows represent all N different antenna positions.

A necessary condition, especially for the following MUSIC algorithm is that the estimated sampled covariance matrix has to be of full rank. There are different

ways to achieve this with a single snapshot model. The best suited method for this specific measurement is to implement a smoothing technique introduced in [25]. This smoothing technique chooses the channel state information of a N-size antenna array at different subcarrier indices and stacks them into matrix $\tilde{\mathbf{H}}^{N \times L}$. As an example, Fig. 9 illustrates the generation of the matrix $\tilde{\mathbf{H}}$ for an array with the size of $N = 4$ and $N_{sub} = 7$ subcarriers.
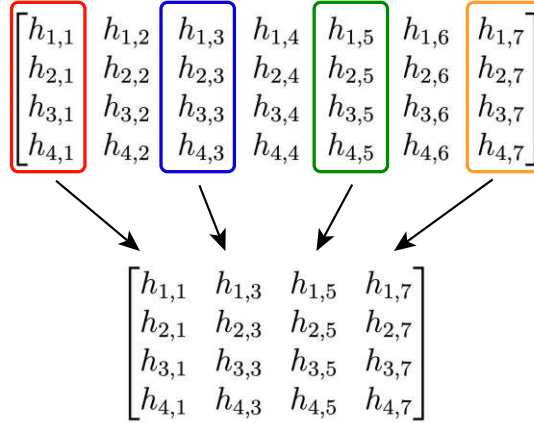
$$
\begin{bmatrix}
h_{1,1} & h_{1,2} & h_{1,3} & h_{1,4} & h_{1,5} & h_{1,6} & h_{1,7} \\
h_{2,1} & h_{2,2} & h_{2,3} & h_{2,4} & h_{2,5} & h_{2,6} & h_{2,7} \\
h_{3,1} & h_{3,2} & h_{3,3} & h_{3,4} & h_{3,5} & h_{3,6} & h_{3,7} \\
h_{4,1} & h_{4,2} & h_{4,3} & h_{4,4} & h_{4,5} & h_{4,6} & h_{4,7}
\end{bmatrix}
$$

$$
\begin{bmatrix}
h_{1,1} & h_{1,3} & h_{1,5} & h_{1,7} \\
h_{2,1} & h_{2,3} & h_{2,5} & h_{2,7} \\
h_{3,1} & h_{3,3} & h_{3,5} & h_{3,7} \\
h_{4,1} & h_{4,3} & h_{4,5} & h_{4,7}
\end{bmatrix}
$$

Figure 9: Illustration of the generation of the $\tilde{\mathbf{H}}$ matrix. For this example, an array size of $N = 4$ with $N_{Sub} = 7$ subcarriers is chosen. To generate a full-rank correlation matrix a minimum of $L = 4$ subcarriers is needed.

The number of chosen subcarriers L must be at least as large as the number of antennas N to generate a full rank correlation matrix. In the measurement scenario, I considered $L = 144$ different subcarriers, with a maximum spacing between these subcarriers over the whole bandwidth. This results in a spatial covariance matrix with full rank. Note that the different subcarriers have to be independent. A further increase of the subcarrier considered for frequency smoothing does not lead to an improved result for DOA estimation. The sample covariance matrix can now be estimated with

$$
\hat{\mathbf{R}}_{hh} = \frac{1}{L} \tilde{\mathbf{H}} \tilde{\mathbf{H}}^{\mathsf{H}} . \tag{16}
$$

After estimating the sampled covariance matrix, I can calculate the angular power spectrum of the Bartlett beamformer with

$$
P_{\mathsf{BF}}(\varphi) = \frac{\mathbf{a}(\varphi)^{\mathsf{H}} \hat{\mathbf{R}}_{hh} \mathbf{a}(\varphi)}{\mathbf{a}(\varphi)^{\mathsf{H}} \mathbf{a}(\varphi)} . \tag{17}
$$

In my application, I find the P highest peaks of $P_{\text{BF}}(\varphi)$ by employing a simple peakfinding algorithm. This angle of the occurring peaks corresponds to the P strongest DOAs.

In [26] the performance of the Bartlett beamformer is studied. The algorithm is scanning a conventional beam. Two plane waves are considered resolvable if the peak of the second beam pattern lies at or outside of the null of the first beam pattern [22]. The null-to-null beamwidth is defined as

$$BW_{NN} = 2\frac{\lambda}{Nd}. \tag{18}$$

The distance to the first null is one half of the null-to-null beamwidth and is called the Rayleigh resolution limit. That means that I am able to resolve targets, which are separated by $\frac{1}{2}BW_{NN} = \frac{\lambda}{Nd} = \frac{1}{0.4N} \approx 0.017$rad in the measurement setup presented in this thesis. This corresponds to an angle of $\approx 1°$.

There are various modifications of the Bartlett beamformer for the different areas of applications. One can, for example, improve the resolution by adding external weighting. In this work, I only consider the standard Bartlett beamformer without further modifications because the main focus of this thesis is to investigate the influence of motion.

2.4.2   MUltiple SIgnal Classification (MUSIC)

The conventional beamformer produces large side-lobes, which reduce the ability to reliably identify two closely spaced DOAs [27]. Nowadays, sub-space oriented methods are commonly used because of their high resolution compared to the beamspace algorithms [28]. Sub-space methods, as for example the MUSIC algorithm, are based on the eigen-structure of the covariance matrix [22]. The special structure of the covariance matrix and the spatial white noise assumption lead to the spectral eigenvalue decomposition

$$\hat{\mathbf{R}}_{\text{hh}} = \sum_{i=0}^{N} \hat{\lambda}_i \hat{\mathbf{u}}_i \hat{\mathbf{u}}_i{}^{\text{H}}, \tag{19}$$

where $\hat{\lambda}_i$ is the i-th eigenvector of the estimated channel correlation matrix and $\hat{\mathbf{u}}_i$ is

the corresponding eigenvector. This equation can also be represented in matrix form as

$$\hat{\mathbf{R}}_{\mathsf{hh}} = \hat{\mathbf{U}}\hat{\Lambda}\hat{\mathbf{U}}^{\mathsf{H}},$$ (20)

with $\hat{\Lambda} = \mathrm{diag}\{\hat{\lambda}_1, \hat{\lambda}_1, \ldots \hat{\lambda}_N\}$ and $\hat{\mathbf{U}}$ containing all eigenvectors stacked together into a matrix. The eigenvalues are assumed to be in the order of decreasing size ($\lambda_1 \geq \lambda_2 \geq \cdots \geq \lambda_N$). The first P eigenvalues,

$$\hat{\lambda}_i \quad i = 1, 2, \ldots, P$$ (21)

refer to the signal-subspace eigenvalues and

$$\hat{\mathbf{u}}_i \quad i = 1, 2, \ldots, P$$ (22)

to the signal-subspace eigenvectors. The remaining $N - D$ eigenvalues and eigenvectors define a noise-space that does not contain any signal components. In the signal-subspace there is also a noise component. The signal sub-space

$$\hat{\mathbf{U}}_S = \begin{bmatrix} \hat{\mathbf{u}}_0 & \hat{\mathbf{u}}_1 & \ldots & \hat{\mathbf{u}}_P \end{bmatrix}$$ (23)

is defined as a $N \times P$ matrix and the noise-space

$$\hat{\mathbf{U}}_N = \begin{bmatrix} \hat{\mathbf{u}}_{P+1} & \hat{\mathbf{u}}_{P+2} & \ldots & \hat{\mathbf{u}}_N \end{bmatrix}$$ (24)

is defined as a $N \times (N - P)$ matrix. All eigenvectors are orthogonal to $\mathbf{a}[\varphi]$ for all DOAs $\varphi_1, \varphi_2 \ldots \varphi_P$. This can be written as

$$\|\mathbf{a}[\varphi]^{\mathsf{H}}\hat{\mathbf{U}}_N\| = 0.$$ (25)

The MUSIC algorithm utilizes this property by calculating the "angular power spectrum" with

$$P_{\mathsf{MUSIC}}[\varphi] = \frac{1}{\sum_{i=p+1}^{N} |\mathbf{a}[\varphi]^{\mathsf{H}}\mathbf{u}_i|^2} \ .$$ (26)

The orthogonality condition of (25) generates peaks in the angular power spectrum at the location of the estimated angles $\hat{\varphi}_1, \hat{\varphi}_2 \ldots \hat{\varphi}_P$. As mentioned in the last section,

the estimate of the correlation matrix has to be a full rank matrix. A rank deficit in the correlation matrix means that the eigenvectors are not independent of each other. This results in a divergence of a signal eigenvector into the noise subspace. This generally leads to $\|\mathbf{a}(\varphi)^{\mathsf{H}}\hat{\mathbf{U}}_N\| \neq 0$ for any φ, which will result in a dramatically reduced resolvability of closely spaced DOAs. In the worst case, the MUSIC algorithm will fail to produce peaks at the correct DOA location.

2.5 Measurement Results

In this section, I will present the DOA estimation results of the Bartlett beamformer and the MUSIC algorithm for all six scenarios mentioned in Section 2.1. The first subsection contains the results of the standstill measurements at both frequencies (Scenario E and Scenario F). The same algorithms are then utilized for the measurements in motion. In the last subsection, I will compare the standstill measurement results with the measurement results at different movement speeds.

2.5.1 Standstill Measurements

To get a first impression of the number of multi-path components (MPC)s, I plot the absolute eigenvalues of the sample covariance matrix $\hat{\mathbf{R}}_{\mathsf{hh}}$. Figure 6 shows the 50 strongest absolute eigenvalues in dB of the $2.55\,\mathrm{GHz}$ and the $25.5\,\mathrm{GHz}$ measurements. At both frequencies, two dominant paths can be identified. Between the second and the third eigenvalue, there is a decrease of $1 - 2\mathrm{dB}$ in terms of absolute value. The following eigenvalues are less descending. After the eight strongest eigenvalues, there is a small step in both scenarios. In the mmWave scenario the absolute values are then descending much smoother than in the sub $6\,\mathrm{GHz}$ case. To separate the signal from the noise space, I introduce a threshold of $-4\,\mathrm{dB}$. All eigenvalues above this threshold are considered to lie in the signal space (shown as red dots in the figure) and the remaining eigenvalues are considered to be in the noise-space. In Scenario E, $P = 12$ signals are above the given threshold and in Scenario F, only eight eigenvalues lie above this threshold.

With the algorithm introduced in the previous section, I calculate the angular power spectrum for both standstill scenarios. The result of the Bartlett beamformer is shown in Fig. 11 and for the MUSIC algorithm in Fig. 12. For a better spatial imagination, the estimated angular power spectrum is first shown in a polar coordinate system.
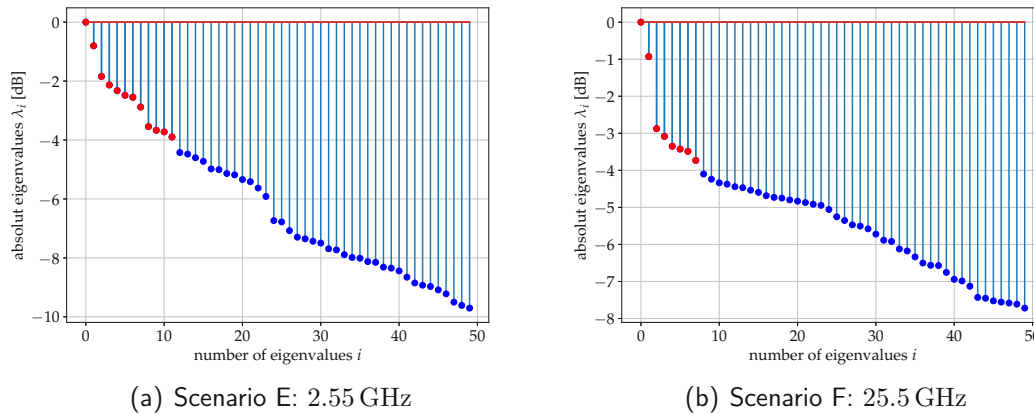
(a) Scenario E: $2.55\,\mathrm{GHz}$ (b) Scenario F: $25.5\,\mathrm{GHz}$

Figure 10: The first 50 absolute eigenvalues of Scenario E and Scenario F. The two scenarios have similar behavior with two very dominant eigenvalues. The decision threshold is given at $-4\mathrm{dB}$. Eigenvectors corresponding to the signal space are marked in red.

First, I focus on the analysis of Scenario F. The dominant MPCs travel through the wall and the closed door (see Fig. 1 for the floorplan). The power difference of the individual paths is less than $0.5\,\mathrm{dB}$, which makes DOA estimation difficult. Especially for the conventional beamformer, it is hard to differentiate between closely spaced directions. The high number of scattering objects in an office environment can lead to a higher incidence of closely spaced DOAs. There is a similar behavior in Scenario E. The dominant waves are also traveling through the wall, but there is also a large component at approximately $70°$.

To compare the results of the implemented DOA estimation methods, I depict the results on a linear scale in Fig. 13. The two scenarios provide the same results. The angular power spectrum matches or comes close to each other to a large extent. The power spectrum estimated by the MUSIC algorithm is not a true spectrum in any sense. It is merely the distance between two subspaces. Therefore, it is hard to compare the amplitudes of the angular power spectrum. Rather of interest are the exact locations of the P dominant paths. These locations are determined by a peakfinding algorithm conducted in Python. The P strongest paths are shown in Tab. 2. The side-lobes caused by the Bartlett beamformer generate additional, slightly smaller paths in the near vicinity of the actual path. A side-lobes of a DOA can be larger than an other weaker DOA. By taking only the strongest P paths into account, can lead to a wrong detection by the peakfinding algorithm. It is possible that the peakfinding algorithm choose a side-lobe instead of a weaker DOA. This explains the difference of between DOAs listed in Tab. 2. The same DOAs are indicated in boldface.

(a) Scenario E: 2.55 GHz   (b) Scenario F: 25.5 GHz
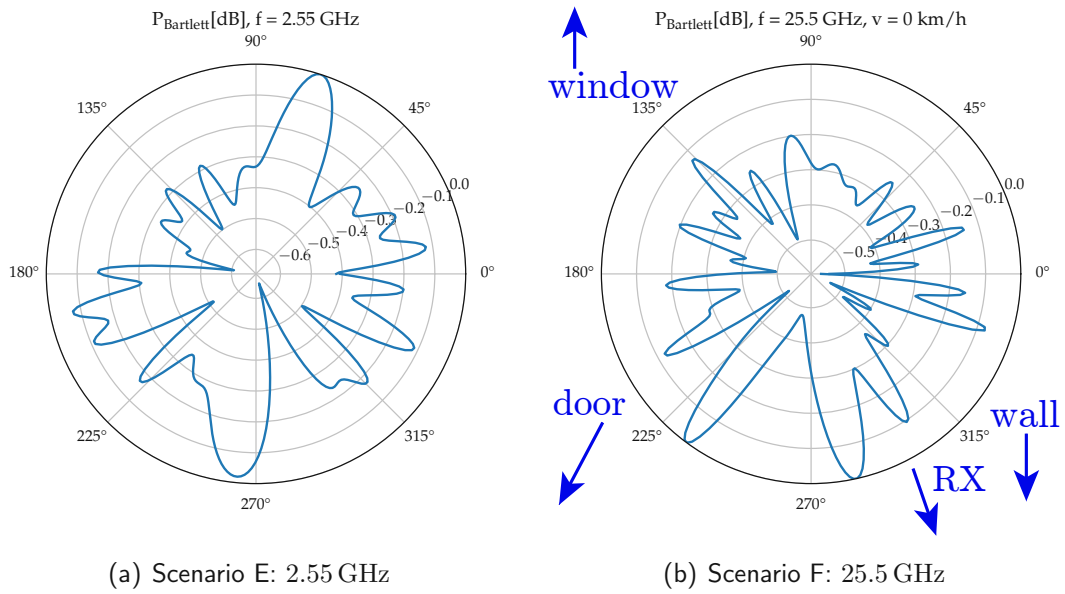
Figure 11: Angular power spectrum estimated with an Bartlett beamformer.

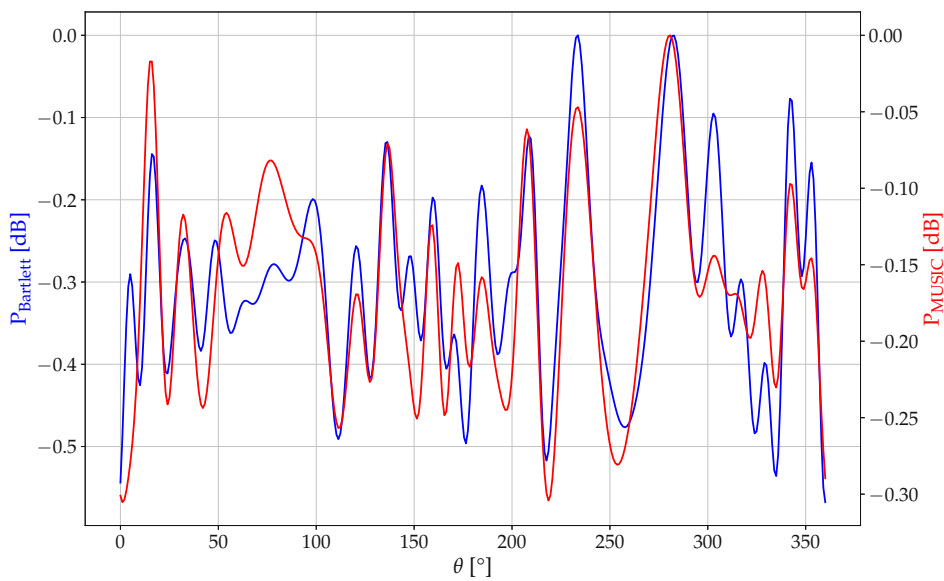(a) Scenario E: 2.55 GHz   (b) Scenario F: 25.5 GHz
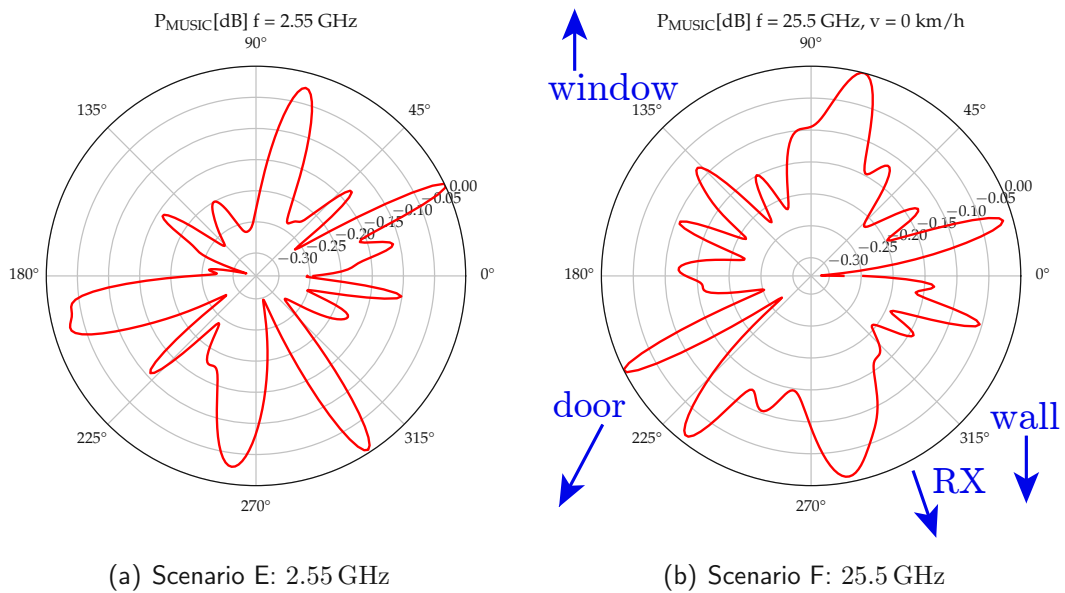
Figure 12: Angular power spectrum estimated with the MUSIC algorithm
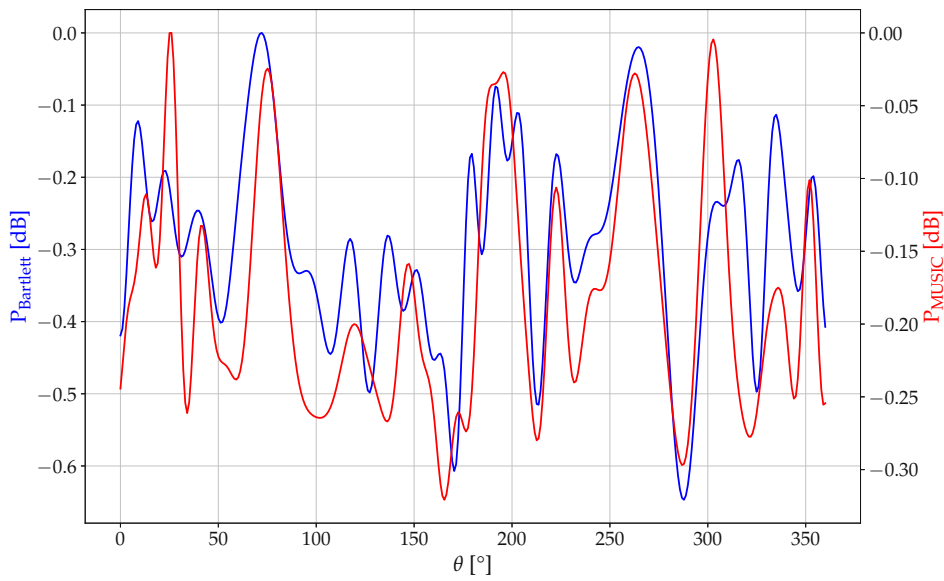
(a) Scenario E: $2.55\,\mathrm{GHz}$

(b) Scenario F: $25.5\,\mathrm{GHz}$

Figure 13: Comparison of the estimated angular power spectrum estimated by the Bartlett beamformer and the MUSIC algorithm for the standstill scenarios.

Scenario E:

$\varphi_{\mathbf{p}}[^\circ]$	φ_1	φ_2	φ_3	φ_4	φ_5	φ_6	φ_7	φ_8	φ_9	φ_{10}	φ_{11}	φ_{12}
Bartlett	**9**	**23**	**72**	179	**191**	**202**	**222**	264	**304**	315	334	**353**
MUSIC	**5**	18	**27**	41	**77**	118	**193**	**204**	**221**	258	**303**	**352**

Scenario F:

$\varphi_{\mathbf{p}}[^\circ]$	φ_1	φ_2	φ_3	φ_4	φ_5	φ_6	φ_7	φ_8
Bartlett	**16**	136	**208**	**233**	**282**	302	**341**	352
MUSIC	**16**	75	**136**	**206**	**231**	249	**280**	343

Table 2: DOA estimates provided by a peakforming algorithm for both standstill scenarios

2.5.2   Measurement in Motion

The whole estimation procedure stays the same for the motion measurements. I choose the same number of DOAs as in the standstill scenarios ($P = 12$ for $f_c = 2.55\,\mathrm{GHz}$ and $P = 8$ for $f_c = 2.55\,\mathrm{GHz}$), because the measurement is static so the number of propagation paths should stay the same. Figure 14 shows the result of the two DOA estimates at speeds of $20\,\mathrm{km/h}$ and $200\,\mathrm{km/h}$. The behavior of the Bartlett beamformer in comparison to the MUSIC algorithm is the same as in the standstill scenarios. The MUSIC algorithm has a better angular resolution than the Bartlett beamformer. By adding motion to the measurement, the angular power spectrum and the estimated DOAs change dramatically. The angular power is spread across all possible directions compared to the standstill measurements. In the stanstill scenarios, one can determine a main direction of the incoming paths. With the spreaded spectrum in the motion scenarios, this is not longer possible. The red and the green curves in Fig. 14 represent one velocity each. They show similar behavior and the shape of the angular power spectrum at both velocities look similar as well. The components, however, have a different signal strength depending on the velocity. With a closer examination, one can also see a slight angular shift. The results of the P strongest paths determined by the peakfinder are summarized in Tab. 3. Hardly any estimated DOA is the same as in the standstill case. I marked the similar DOAs compared with the standstill scenario in Tab.3. Because it is hard to evaluate the error by only looking at the estimated DOAs, I introduce the circular variance and the angular mean in the next section.
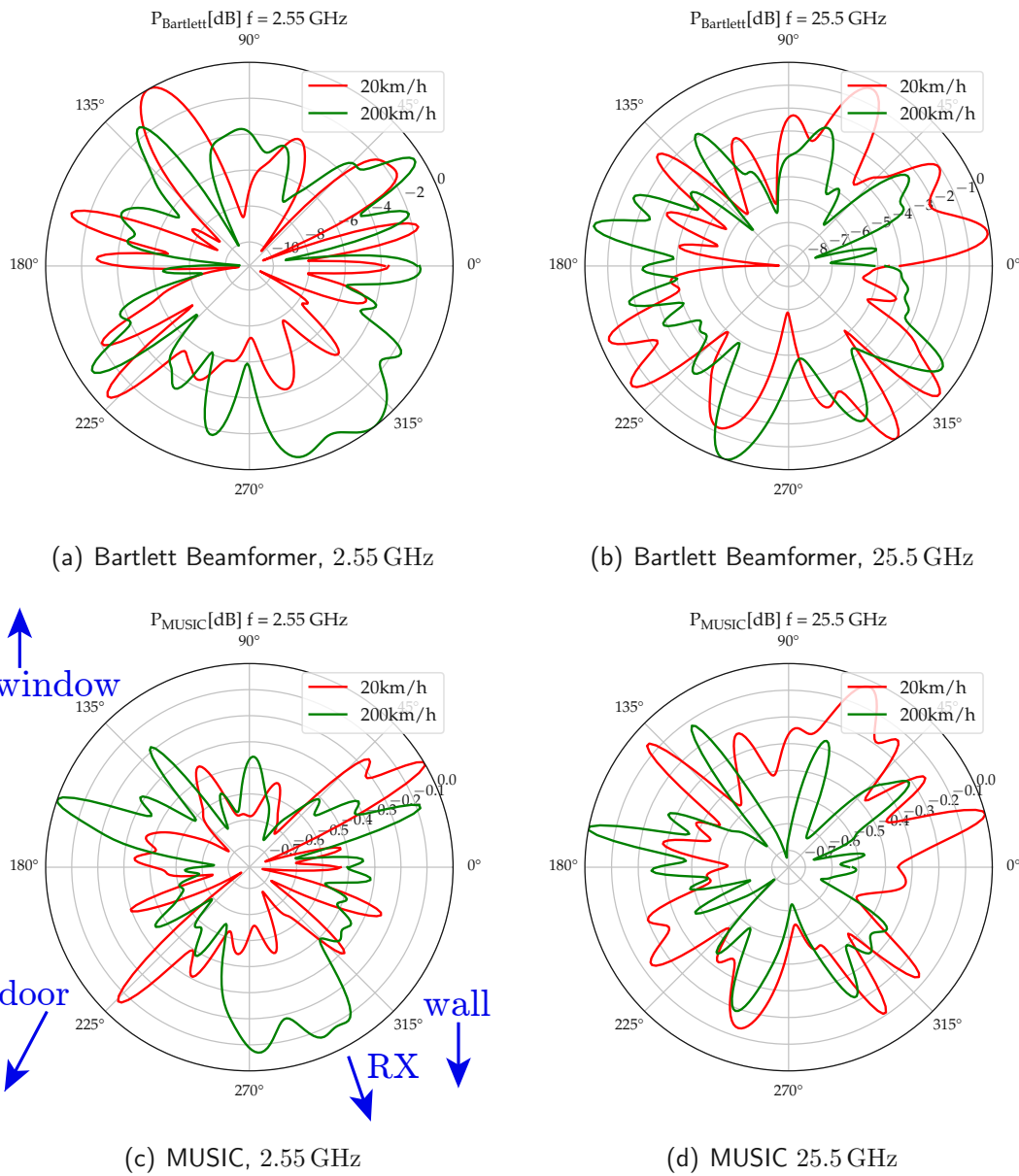
(a) Bartlett Beamformer, 2.55 GHz

(b) Bartlett Beamformer, 25.5 GHz

(c) MUSIC, 2.55 GHz

(d) MUSIC 25.5 GHz

Figure 14: Angular power spectrum estimated with a Bartlett beamformer and MUSIC algorithm.

Scenario A:

$f_c = 2.55\,\mathrm{GHz}$

$v = 20\,\mathrm{km/h}$

$\varphi_{\mathbf{p}}[^\circ]$	φ_1	φ_2	φ_3	φ_4	φ_5	φ_6	φ_7	φ_8	φ_9	φ_{10}	φ_{11}	φ_{12}
Bartlett	**13**	33	**68**	119	163	**177**	207	**222**	245	286	**314**	343
MUSIC	11	**31**	**42**	**117**	163	175	**200**	**225**	242	286	317	339

Scenario B:

$f_c = 2.55\,\mathrm{GHz}$

$v = 200\,\mathrm{km/h}$

$\varphi_{\mathbf{p}}[^\circ]$	φ_1	φ_2	φ_3	φ_4	φ_5	φ_6	φ_7	φ_8	φ_9	φ_{10}	φ_{11}	φ_{12}
Bartlett	**18**	33	44	128	157	213	238	257	285	**307**	329	**358**
MUSIC	**3**	**19**	31	129	147	160	272	293	**301**	320	329	**353**

Scenario C:

$f_c = 25.5\,\mathrm{GHz}$

$v = 20\,\mathrm{km/h}$

$\varphi_{\mathbf{p}}[^\circ]$	φ_1	φ_2	φ_3	φ_4	φ_5	φ_6	φ_7	φ_8
Bartlett	9	33	65	202	217	246	**301**	319
MUSIC	**15**	49	66	**139**	215	**252**	303	319

Scenario D:

$f_c = 25.5\,\mathrm{GHz}$

$v = 200\,\mathrm{km/h}$

$\varphi_{\mathbf{p}}[^\circ]$	φ_1	φ_2	φ_3	φ_4	φ_5	φ_6	φ_7	φ_8
Bartlett	35	125	156	168	192	251	295	325
MUSIC	35	**73**	124	156	169	181	**249**	297

Table 3: DOA estimates provided by a peakforming algorithm for all movement scenarios

2.5.3 Circular Variance and Angular Mean

The angular mean indicates the angle at which, on average, the most power is concentrated.
The mean angle $\bar{\varphi} \in \mathbb{C}$ is defined by

$$\bar{\varphi} = \int_0^{2\pi} e^{j\varphi} P(\varphi) \mathrm{d}\varphi, \tag{27}$$

where $P(\varphi)$ is the direction power spectrum, calculated through

$$P(\varphi) = \frac{P_{\mathsf{BF}}(\varphi)}{\int_0^{2\pi} P_{\mathsf{BF}}(\varphi)\mathrm{d}\varphi}. \tag{28}$$

or

$$P(\varphi) = \frac{P_{\mathsf{MUSIC}}(\varphi)}{\int_0^{2\pi} P_{\mathsf{MUSIC}}(\varphi)\mathrm{d}\varphi}. \tag{29}$$

depending on the applied estimation method. The angular power spectrum $P_{\mathsf{BF}}(\varphi)$ and $P_{\mathsf{MUSIC}}(\varphi)$ are obtained by (17) and (26).

The circular variance σ_φ^2 indicates the variation of the angles around the mean direction, with a possible range between zero and one. A circular variance of one means that the DOAs are uniformly distributed between 0 and 2π. If the circular variance is zero, there is only one angle where the DOAs are focused. There are different definitions of the angular variance. In the field of telecommunication, often the definition of [29] is used due to the fact that it is comparable with the definition of the Doppler and delay spread.

The circular variance is defined by

$$\sigma_\varphi^2 = \int_0^{2\pi} |e^{j\varphi} - \bar{\varphi}|^2 P(\varphi)\mathrm{d}\varphi \tag{30}$$

$$= 1 - |\bar{\varphi}|^2. \tag{31}$$

Table 4 shows the calculated results of the mean direction and circular variance for the $2.55\,\mathrm{GHz}$ measurement and Tab. 5 for the $25.5\,\mathrm{GHz}$ measurement.

The angular variance is very high in all cases and approaching $\sigma_\varphi^2 = 1$. This is caused by the very small power difference in the angular spectrum. In the case of DOA estimation with the MUSIC algorithm, there is only a maximum difference of $0.3\,\mathrm{dB}$ in the amplitude of the angular spectrum. The angular variance of the Bartlett beamformer is slightly smaller. At first, this seems to make no sense because the

spectrum in the standstill scenario seems to have a much higher directivity than the spectrum in the motion scenario. At a second glance, it can be seen that the power difference between the strongest and weakest path increases from $0.5\,\mathrm{dB}$ to $8-10\mathrm{dB}$ by adding motion to the experiment. This explains the decreasing angular variance.

The more interesting variable is the angular mean. Here, the comparison between the two algorithms makes little sense because the side-lobes generated by the Bartlett beamformer change the angular mean, but it gives a good indication of how much the angular power spectrum change by adding motion to the measurement.

I calculate the error in the mean angle at velocity v with

$$\epsilon_v[°] = \min(|\measuredangle\ \bar{\varphi}_0 - \measuredangle\ \bar{\varphi}_v|, 360° - |\measuredangle\ \bar{\varphi}_0 - \measuredangle\ \bar{\varphi}_v|) \tag{32}$$

where $\bar{\varphi}_0$ is the mean angle at standstill and $\bar{\varphi}_v$ is the mean angle at velocity v. The possible range of ϵ_v is between $0°$ and $180°$. This means that the maximal error occurs if the mean angle is shifted by $180°$.

Table 6 shows the calculated error in degree and in percent for all algorithms and frequencies. The error has a big range of fluctuation, going from only 3.9% up to 56%. For most of the scenarios, the error of the angular mean is very high. In all scenarios, the error gets higher with increasing velocity. For a center frequency of $2.55\,\mathrm{GHz}$, the Bartlett beamformer performs very badly and produces a high error in terms of the angular mean. The MUSIC algorithm works better at a lower frequency but also produces a high error at higher velocity. In the mmWave scenario, the two estimation methods produce a very high error at the measured velocities. Here the MUSIC algorithm performs much worse at a lower velocity than the Bartlett beamformer and has a similar performance at $200\,\mathrm{km/h}$.

To better understand, why the presented DOA estimation algorithm produce this significant error if one antenna is in motion, I replicate the measurement with an simulation. The simulation model is introduced in the following Section.

Bartlett Beamformer

	$\measuredangle\ \bar{\varphi}$	σ_φ^2
standstill	26.22°	0.99997
motion 20 km/h	127.03°	0.99172
motion 200 km/h	311.97°	0.96357

MUSIC Algorithm

	$\measuredangle\ \bar{\varphi}$	σ_φ^2
standstill	331.69°	0.99997
motion 20 km/h	335.60°	0.99465
motion 200 km/h	303.78°	0.98862

Table 4: Calculated angular mean and circular variance for the $2.55\,\mathrm{GHz}$ measurement at different velocities. The angular power spectrum is estimated by a Bartlett beamformer and with MUSIC

Bartlett Beamformer

	$\measuredangle\ \bar{\varphi}$	σ_φ^2
standstill	313.91°	0.99999
motion 20 km/h	342.58°	0.99465
motion 200 km/h	242.05°	0.98862

MUSIC Algorithm

	$\measuredangle\ \bar{\varphi}$	σ_φ^2
standstill	334.47°	0.99999
motion 20 km/h	33.59°	0.99992
motion 200 km/h	257.50°	0.99998

Table 5: Calculated angular mean and circular variance for the $25.5\,\mathrm{GHz}$ measurement at different velocity. The angular power spectrum is estimated by a Bartlett beamformer and with MUSIC

algorithm	f_c	$\epsilon_{20}[°]$	$\epsilon_{20}[\%]$	$\epsilon_{200}[°]$	$\epsilon_{200}[\%]$
Bartlett	2.55 GHz	34.80°	19.33%	74.25°	41.25%
Bartlett	25.5 GHz	28.66°	15.92%	71.83°	39.92%
MUSIC	2.55 GHz	3.90°	2.16%	27.91°	15.52%
MUSIC	25.5 GHz	59.11°	32.84%	76.97°	42.76%

Table 6: Calculated mean angular error at different frequencies using different algorithms. ϵ_{20} and ϵ_{200} are the errors at a velocity of $20\,\text{km/h}$ and $200\,\text{km/h}$, respectively.

3   Simulation

The measurement results in the last section show that movement of the transmit antenna leads to a change in the estimated angular power spectrum and following an estimation error in terms of estimated DOAs. The movement of the receiving antennas leads to a shift of the received frequency, also known as the Doppler shift. Authors of [30] describe that the superposition of several slightly different Doppler shifted signals leads to a phase shift of the total received signal. This phase shift could lead to a large error in DOA estimation. The Doppler shift is further discussed in Section 3.3. To verify the influence of the Doppler effect on the two presented DOA estimation methods, I create a simulation scenario introduced in Section 3.1. I first implement a time-invariant channel model in Section 3.2, representing the standstill scenario. Taking the Doppler effect into account results in a time-variant channel model introduced in Section 3.3. Until now, the antenna motion during one symbol duration has been neglected because the covered distance during one symbol or snapshot is relatively small in comparison to the distance between transmitter and receiver or scattering object and receiver. This assumption is very common in real world measuring scenarios [31, 32, 33]. This effect might be less significant than the Doppler effect but could led to an error in DOA estimation. The model taking the antenna position change into account is introduced in Section 3.4. To express the error introduced by the antenna movement in a mathematical way, I calculate the error of the estimated mean DOA direction, which is already presented in Section 2.5.3. The results are shown in Section 3.5.1. Further, the influence of the symbol duration is analyzed in Section 3.5.2. In the last section of this chapter, I discuss the simulation results and compare them with the measurement.

3.1   Simulation Scenario

To better understand the measurement results, I create a simulation scenario, which should be as close to the measurement scenario as possible. Identical to the measurement, I consider a SIMO scenario. On the receiver side, I generate the same URA with $N = 144$ receive antennas with $N_x = 18$ antennas in the x-direction and $N_y = 8$ antennas in the y-direction. The antenna spacing depends on the considered frequency and is chosen to be equal to the measurement $d = 0.4\lambda$. As a simplification, I only consider the path from different scattering objects to the receiving antennas and neglect the path from the transmitter to the receiver. The transmit antenna location is not necessary for this simulation because only the DOAs are of interest. This basically means that I consider a pure non-line-of sight (NLOS) scenario. This is similar to the measurement scenario because a wall blocks the direct path. I assume that the re-radiation at the scatterer is isotropic. Further, I assume that only one wave is re-radiated at each scattering object p with a scattering gain of g_p.

To get a spacial consistent channel model, each antenna element and each scatterer are assigned with an explicit location. Every antenna element i of the URA can be represented by a 2-dimensional position vector $\mathbf{r}_{ant,i} = \begin{bmatrix} x_{ant,i} & y_{ant,i} \end{bmatrix}^\mathsf{T}$, where $x_{ant,i}$ is the position of antenna i on the x-axis and $y_{ant,i}$ on the y-axis. The first antenna element is placed at the origin ($\mathbf{r}_{ant,1} = \begin{bmatrix} 0 & 0 \end{bmatrix}^\mathsf{T}$). The location of the other antennas result from the given antenna array form and the antenna spacing. For this simulation $P = 3$ different scatter locations are considered, where each scatterer can also be described by a position vector $\mathbf{r}_p = \begin{bmatrix} x_p & y_p \end{bmatrix}^\mathsf{T}$. Each position vector (antenna and scatterer) can also be represented with polar coordinates where $\|\mathbf{r}_p\|$ indicates the distance to the the p-th scattering object and φ_p is the azimuth angle. This angle φ_p represents the DOA from the wave re-radiated from this scattering object. Although I only consider a two dimensional approach in this thesis, one can easily extend the simulation to a 3D model. An illustration of the employed simulation scenario is shown in Fig. 15.

As in the measurement, the antenna array is first considered to be static. In the later section of this chapter, the antenna array is in motion with different velocities. The velocity vector is also shown in Fig. 15. Corresponding to Section 2, I choose a constant speed of $20\,\mathrm{km/h}$ and $200\,\mathrm{km/h}$ for the simulation.
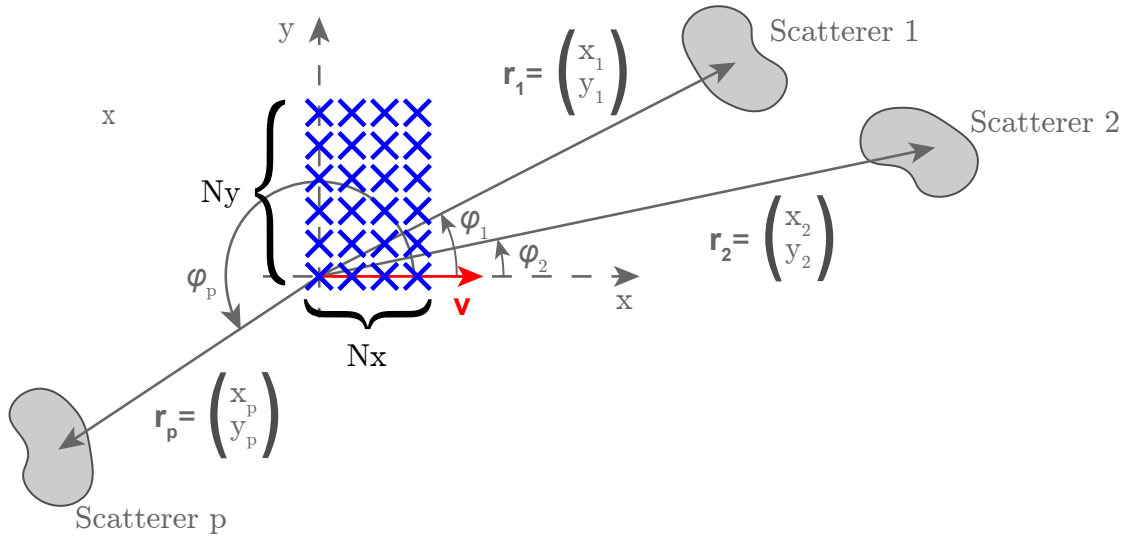
Figure 15: Geometry of the simulation scenario. At the receiver, a URA with $N = 144$ antennas is employed. Each of the P scatterers can be described by a position vector.

3.2   Time-Invariant Channel Model

I first consider that the antenna array is not moving. To simulate the channel for the standstill scenario, I generate a time-invariant channel. Each antenna-scatterer pair has an individual channel coefficient. I assume free space propagation between each scatterer and receiving antenna, which means that there are no additional reflecting or absorbing objects in the path. This allows the implementation of a free space channel model introduced in [34]. This model is a small scale fading model. The free space channel model results in an exact solution in the sense that there is no far-field assumption. The DOA is given by the location of the scatterers $\mathbf{r}_{ant,i}$.

The channel coefficient from antenna element $i \in 1 \dots N$ to scatterer $p \in 1 \dots P$ is given by

$$h_i = \sum_{p=1}^{P} g_p \exp\left(-j \frac{2\pi f_c}{c} \left\| \mathbf{r}_p - \mathbf{r}_{ant,i} \right\| \right). \tag{33}$$

The channel gain of the path coming from scatterer p is referred to as g_p. To verify the behaviour of the change in amplitude of the angular power spectrum at different DOAs for the two estimation techniques, I set all channel gains to the same value. This is usually not the case in a real world scenario. For P number of scatterers, I calculate the channel gains with $g_1 = g_2 = \cdots = g_P = \frac{1}{P}$, leading to a normalized power of $\|h_i\|^2 = 1$ for each subchannel. Calculating the channel coefficient for all antennas and stacking them into a vector results in the simulated time-invariant channel vector $\mathbf{h} = \begin{bmatrix} h_1 & h_2 & \dots & h_N \end{bmatrix}^\mathsf{T}$.

As mentioned in Section 2.4, the estimated channel correlation matrix must have full rank to enable a precise estimation of the DOAs with the chosen algorithms. To achieve that, I transmit $M = 100$ symbols over the channel. The transmit signal $x[m]$ at the time index m is a randomly generated Gaussian signal with a mean of zero ($\mu_x = 0$) and a standard deviation of one ($\sigma_x = 1$). The received signal vector for an N-size antenna array is written as

$$\underbrace{\begin{bmatrix} y_1[m] \\ y_2[m] \\ \vdots \\ y_\mathsf{N}[m] \end{bmatrix}}_{\mathbf{y}[m]} = \underbrace{\begin{bmatrix} h_1 \\ h_2 \\ \vdots \\ h_N \end{bmatrix}}_{\mathbf{h}} x[m] + \mathbf{n}[m]. \tag{34}$$

The noise vector for each antenna element is represented by $\mathbf{n}$. The complex values of the noise vector are Gaussian-distributed with zero mean. I choose a noise power of 0.1 for the simulation which results in a SNR of $10\,\mathrm{dB}$.

The covariance matrix of the received signal is then estimated with

$$\hat{\mathbf{R}}_{\mathbf{yy}} = \frac{1}{M} \sum_{k=1}^{M} \mathbf{y}[m]\mathbf{y}[m]^{\mathsf{H}} \ . \tag{35}$$

This definition of the estimated covariance matrix $\hat{\mathbf{R}}_{\mathbf{yy}}$ is called the narrowband time-domain snapshot model. If $M > N$, it is secured that the resulting covariance matrix has full rank if the transmit signals are independent. For independent samples in time, the narrowband time-domain snapshot model is equivalent to the estimation method applied in (16).

After estimating the sample covariance matrix, the same algorithms as in Section 2.4 are employed for DOA estimation. Figure 16(a) and 16(b) show the results of the angular power spectrum employing the Bartlett beamformer and MUSIC algorithm at a center frequency of $2.55\,\mathrm{GHz}$. For completeness, I also show the results at a center frequency of $25.5\,\mathrm{GHz}$ in 16(c) and 16(d). The green crosses in the figure mark the estimated DOAs found by a peakfinding algorithm. The two estimation methods deliver the exact same DOAs. Although the shape of the angular power spectrum looks identical for both frequencies, the peakfinding algorithm delivers a slightly different result. In the mmWave scenario, the DOAs could be estimated perfectly with no error. At lower frequency, the results show a small error of $1 - 2°$. Increasing the angular resolution would only lead to a minimal improvement. The angular power spectrum shows the large side-lobes of the Bartlett beamformer and also that the MUSIC algorithm has a higher resolution compared to the beamspace method. In the chosen scenario, this is not a problem because the single DOAs are sufficiently separated.

3.3   Time-Variant Channel Model

In general, the delay of different propagation paths can vary over time. This can be caused by movement of the transmit antenna, receive antenna, objects or by a combination of the three. In this simulation, I only assume movement of the antenna array on the receiving side, considered as a constant linear movement along the x-axis. The movement of the receiving antennas leads to a shift of the received frequency, also known as the Doppler shift [35]. The Doppler shift is determined by the velocity in the direction of the wave propagation. (see Fig. 3.3) To stick to a general channel model without using a far-field assumption, the Doppler shift is calculated individually

(a) Bartlett Beamformer, $2.55\,\mathrm{GHz}$

(b) MUSIC, $2.55\,\mathrm{GHz}$

(c) Bartlett Beamformer, $25.5\,\mathrm{GHz}$
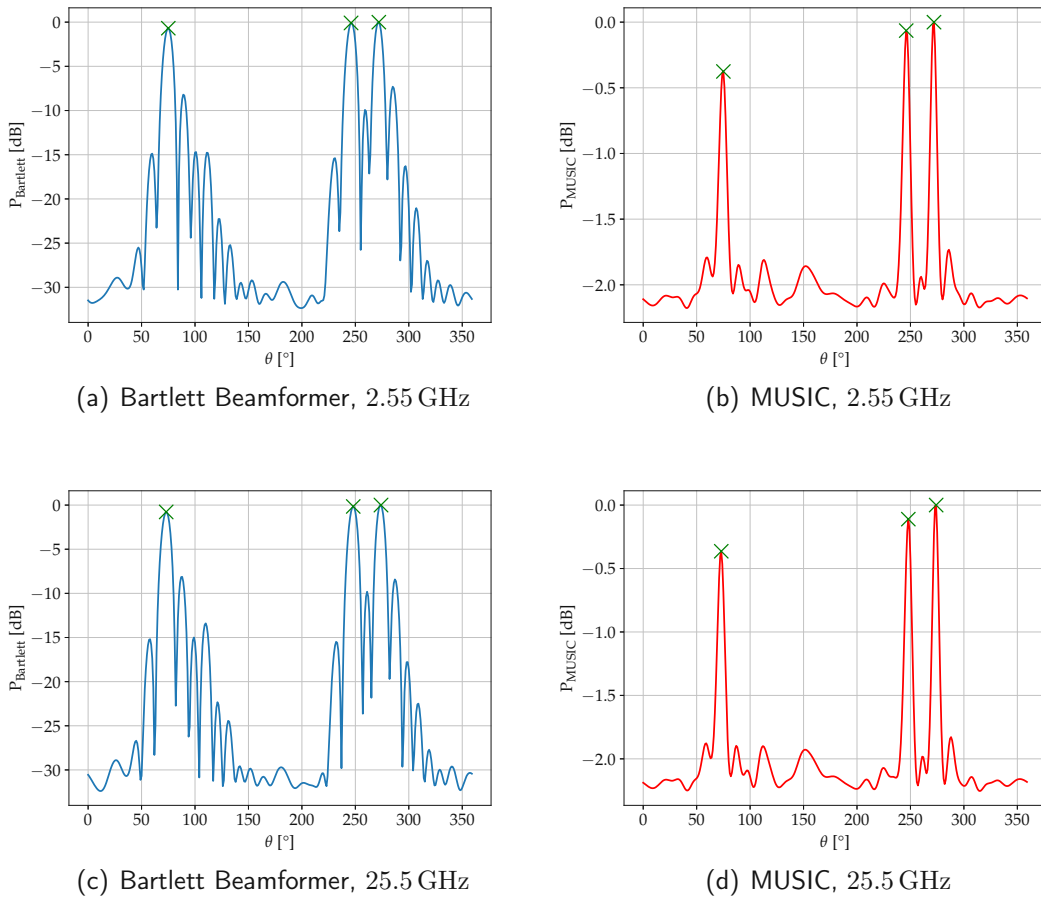
(d) MUSIC, $25.5\,\mathrm{GHz}$

Figure 16: Simulated Angular power spectrum estimated with a Bartlett beamformer and MUSIC algorithm for the time-invariant channel model. The two algorithms provide the same estimates for the DOA. Peakfinding results: $\varphi = \begin{bmatrix} 73 & 248 & 273 \end{bmatrix}^{\mathsf{T}}$ @ f $25.5\,\mathrm{GHz}$, $\varphi = \begin{bmatrix} 75 & 246 & 272 \end{bmatrix}^{\mathsf{T}}$ @ f $2.55\,\mathrm{GHz}$.

for each antenna-scatterer pair. The Doppler shift at antenna i of scatterer p is then calculated by

$$\nu_{i,p} = -\frac{v}{\lambda}\cos(\varphi_{i,p}) = -f_c\frac{v}{c}\cos(\varphi_{i,p}) = -\nu_{max}\cos(\varphi_{i,p}), \tag{36}$$

where $\varphi_{i,p}$ is the angle between the incoming wave of scatterer p on antenna i and the velocity vector **v**, as illustrated in Fig. 17. Since the velocity is always small in comparison to the speed of light, Doppler Shifts are usually relatively small. An increase of the frequency by a factor of ten also results in an increase of the Doppler shift by a factor of ten. In the chosen scenario, the highest Doppler shift is

$\nu_{max} = 4.725\,\mathrm{kHz}$ and occurs at a frequency of $25.5\,\mathrm{GHz}$ and a movement speed of $200\,\mathrm{km/h}$. Note that the relationship $\nu_{max} = f_c \frac{v}{c}$ is only valid with several assumptions -,e.g., static interacting objects, no double reflections on moving objects etc [30]. Since the Doppler shifts are so small, it is fair to ask whether they have an impact on the DOA estimation. If all incoming waves were Doppler shifted to the same extent, this could, for example, be easily compensated by the receiver. The important point, is however, that due to different angles of arrival, every MPC experiences a different Doppler shift. Furthermore, the superposition of several slightly different Doppler shifted signals leads to a phase shift of the total received signal [35]. This phase shift can influence the estimation of the DOAs. Therefore, the Doppler frequency can be an important parameter of the channel even though its value is so small.
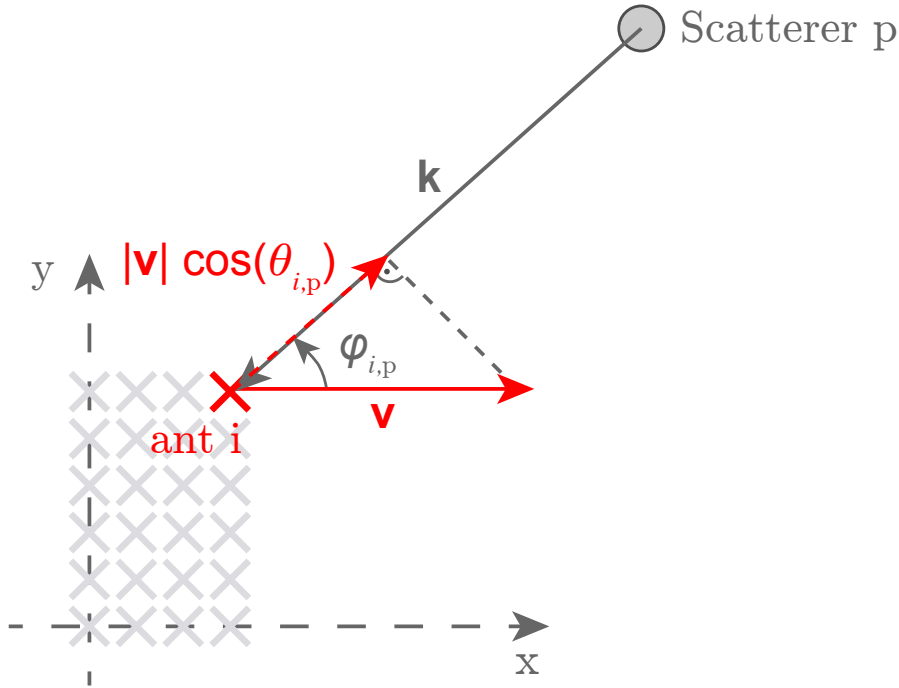
Figure 17: Projection of velocity vector $\mathbf{v}$ onto the direction of propagation $\mathbf{k}$ coming from the p-th scatterer.

Taking into account the Doppler effect, the channel gets time-variant and the channel coefficient at the i-th antenna element at time index m is given as [36]

$$h_i[m] = \sum_{p=1}^{P} g_p \exp\left(-j\frac{2\pi f_c}{c}\|\mathbf{r}_p - \mathbf{r}_{ant,i}\|\right)\exp(j2\pi\nu_{i,p}mT_s), \qquad (37)$$

where T_s denotes the symbol duration. The symbol duration is chosen corresponding
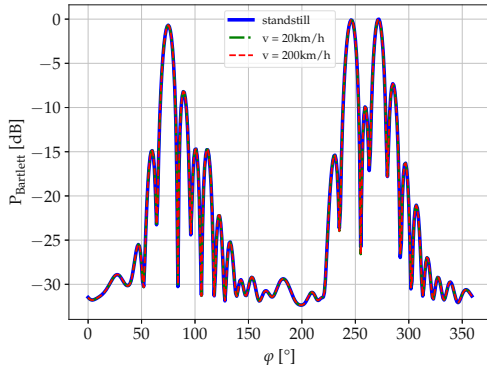
(a) Bartlett Beamformer, $2.55\,\mathrm{GHz}$
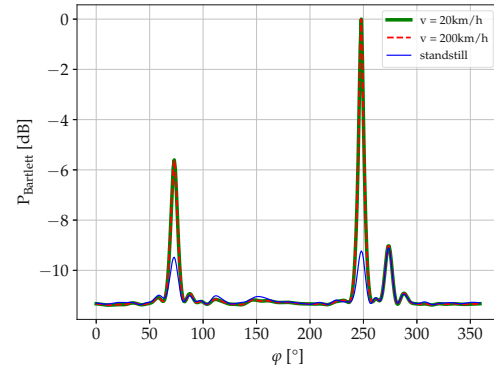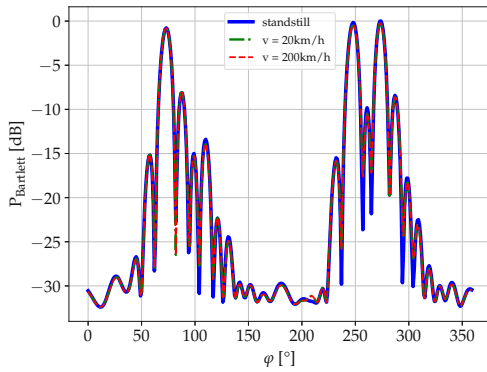
(b) MUSIC, $2.55\,\mathrm{GHz}$

(c) Bartlett Beamformer, $25.5\,\mathrm{GHz}$
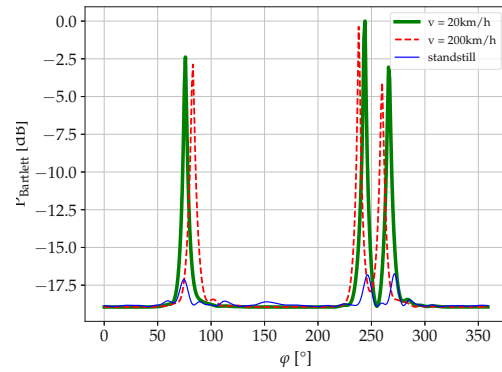
(d) MUSIC, $25.5\,\mathrm{GHz}$

Figure 18: Simulated Angular power spectrum estimated with a Bartlett beamformer and MUSIC algorithm employing a time-variant channel which takes the Doppler shift into account. The Bartlett beamformer shows no change in comparison with the time-invariant channel model. The amplitudes of the spectrum for the MUSIC scenario changes but the angle stays the same.

to the measurement (see Section 5). As in the time-invariant channel model, I use $M = 100$ transmit symbols. The stacked channel matrix $\mathbf{h}[m]$ is now time dependent, which leads to a received signal of

$$\mathbf{y}[m] = \mathbf{h}[m]x[m] + \mathbf{n}[m]. \tag{38}$$

Next, the calculation of the sample covariance matrix and the DOA estimation is done as in Section 3.2.

The angular power spectrum of both, the Bartlett Beamformer and the MUSIC algorithm, is depicted in Fig. 18. In all four scenarios, the value of the DOA estimate is the same as in the time-invariant scenario. This means that considering a Doppler frequency shift does not result in an angular shift of the angular power spectrum. Furthermore, the spectrum shows that the Doppler effect is not influencing the Bartlett beamformer. Regardless of the transmit frequency and velocity, the conventional beamformer delivers the exact same result. On the other hand, in the subspace-technique MUSIC, an amplitude change in the power spectrum can be detected. This amplitude change is first of all depending on the location of the DOA, which is a direct consequence of the angular dependency of the Doppler shift, see (36). Incoming waves which are orthogonal to the movement direction experience no Doppler frequency shift. In the simulation, this is noticeable at the signal component at an angle of $\varphi = 273°$. There, the power is nearly the same as in the standstill scenario. As mentioned before, I assume that independent of the velocity, the antenna array moves the same distance since the symbol rate has been adjusted. Because the ratio of speed and symbol duration stays the same, the algorithms deliver the same results. The amplitude change of the angular power spectrum utilizing the MUSIC algorithm also depends on the transmit frequency. Comparing the MUSIC results at different frequencies, it is evident that the effect becomes stronger. The largest difference between the components increases from approximately $1.5\,\mathrm{dB}$ to $9\,\mathrm{dB}$. It is important to acknowledge that in the chosen simulation scenario all three components should have the same signal strength. This effect is caused by the increased Doppler shift at a higher frequency.

3.4   Time-Variant Antenna Position

The simulation scenario presented in Section 3.1, $M = 100$ symbols are transmitted and the symbol duration of each symbol is given by T_s. If the receiving antenna array is in motion, the antenna is traveling for a distance of $d = vT_s$ during one symbol duration. In real world scenarios, the position change of the antenna array during motion is usually not taken into account [37, 38]. This is due the aspect that the covered distance during one symbol or snapshot is relatively small in comparison to the distance between transmitter and receiver or scattering object and receiver. Since the proposed algorithm is originally intended for a static environment, I investigate the influence of the changing antenna position on the DOA estimation in the following section.

By taking into account the antenna position change due to motion, the position vector $\mathbf{r}_{ant,i}$ gets time variant. The position vector of antenna element i at time instance m can be written as

$$\mathbf{r}_{ant,i}[m] = \mathbf{r}_{ant,i} + \mathbf{v}mT_s. \tag{39}$$

Here, $\mathbf{v} = \begin{bmatrix} v_x & v_y \end{bmatrix}^{\mathsf{T}}$ is the velocity vector. It represents the rate of change of the position of the antenna array in the x and y-direction. In the proposed simulation, the antenna array is moving along the x-axis. This simplifies the velocity vector to $\mathbf{v} = \begin{bmatrix} v & 0 \end{bmatrix}^{\mathsf{T}}$.

Due to the fact that the antenna position is now time dependent, the angular difference between the antennas and scattering objects also change in time. Consequently the Doppler shift is given by

$$\nu_{i,p}[m] = -f_c \frac{v}{c} \cos(\varphi_{i,p}[m]) = -\nu_{max} \cos(\varphi_{i,p}[m]). \tag{40}$$

Inserting the time dependent antenna position $\mathbf{r}_{ant,i}[m]$ and the time dependent Doppler shift $\nu_{i,p}[m]$ into (37), this leads to

$$h_i[m] = \sum_{p=1}^{P} g_p \exp\left(-j\frac{2\pi f_c}{c} \|\mathbf{r}_p - \mathbf{r}_{ant,i}[m]\| \right) \exp(j2\pi\nu_{i,p}[m]mT_s). \tag{41}$$

Next, the obtained channel vector is then used for DOA estimation as in the sections before.

First, I will discuss the Bartlett beamformer results. Simulation results are shown in Fig. 19, where 19(a) and 19(b) show the result for $f_c = 2.55\,\mathrm{GHz}$ and 19(c) and 19(d) for $f_c = 25.5\,\mathrm{GHz}$. The blue curve shows the original estimation at standstill in all four pictures. The movement of the antennas leads to an angular shift of the angular power spectrum. Depending on the movement speed of the receiving antenna, the size of the angular shift changes. At lower velocity, the DOAs are relocated by about $2-4°$. This angular change increases up to about $10°$ at a speed of $200\,\mathrm{km/h}$. The direction in which the component is shifted depends on the initial angle of the incoming wave. The two closer spaced DOAs in the simulation, which were originally located at $248°$ and $273°$ move towards each other reducing their distance. For closely spaced components, this could lead to an overlay, which entails that the single DOA cannot be reliably identified. This further decreases the already bad performance of the Bartlett beamformer in terms of resolution. The overlay of two weaker components or side-lopes could also result in a new DOA at a wrong position. By increasing the number of DOAs, the possibility of overlapping components also extends. As a consequence, the Bartlett beamformer could lead to a high error in terms of angular power spectrum and estimated DOA. The comparison of the angular power spectrum by applying a conventional beamformer at the same velocity but at different frequencies leads only to a very small change in amplitude and circular shift. As mentioned in the previous sections, the Bartlett beamformer results are
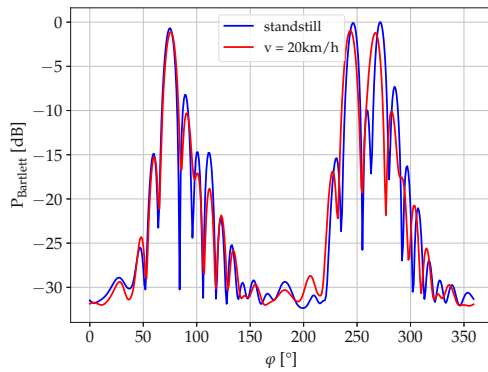
(a) 2.55 GHz, 20 km/h
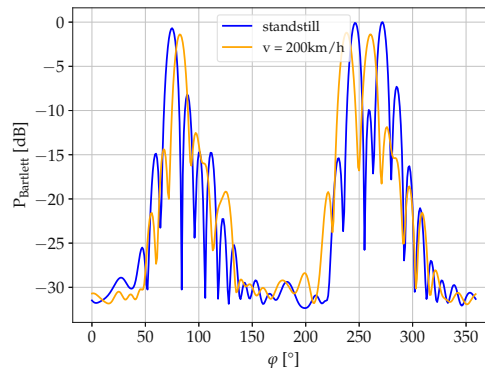
(b) 2.55 GHz, 200 km/h
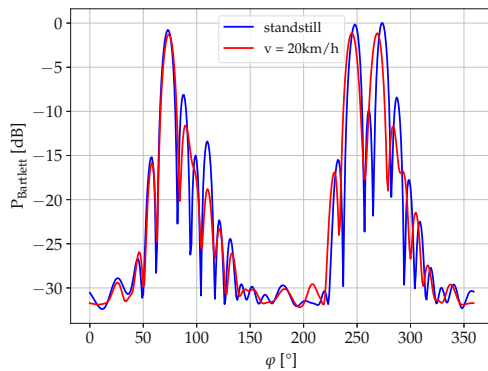
(c) 25.5 GHz, 20 km/h
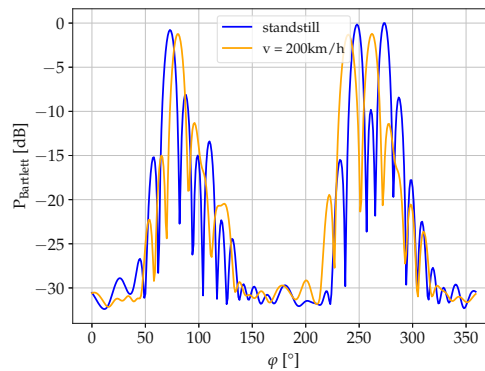
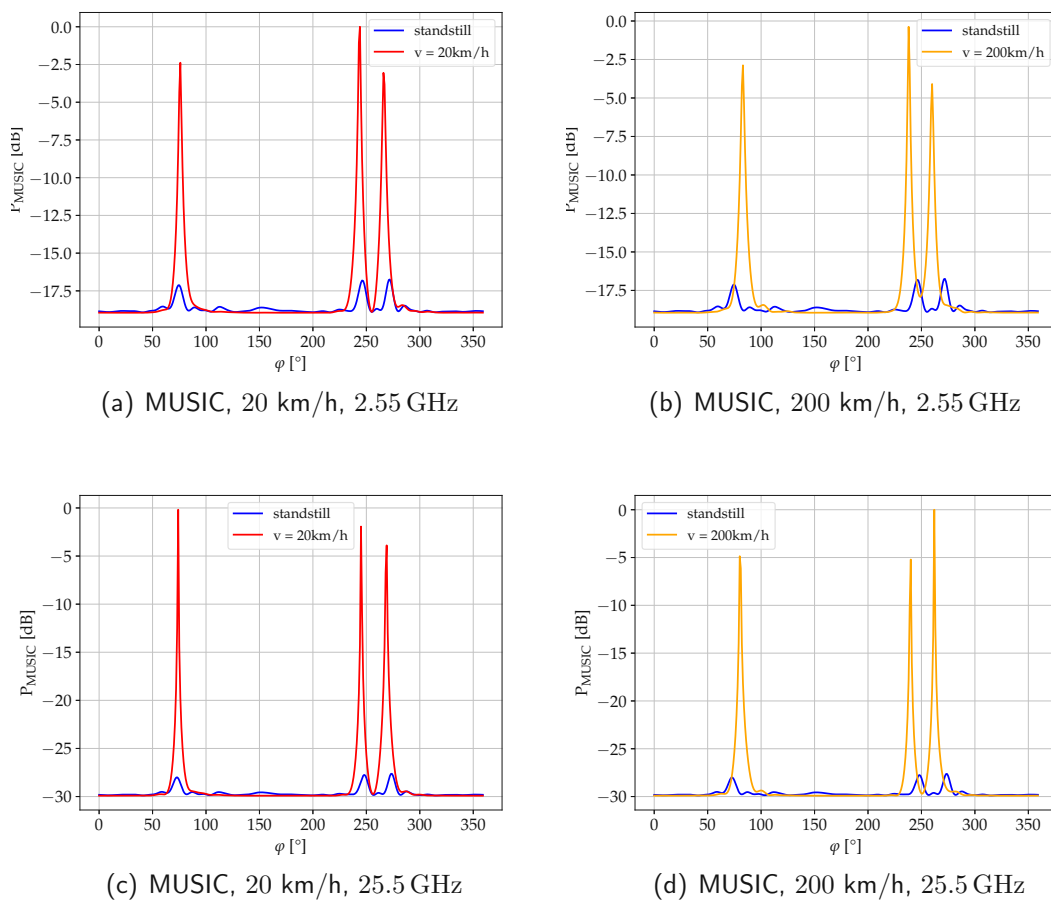(d) 25.5 GHz, 200 km/h

Figure 19: Bartlett beamformer result at $f_c = 2.55\,\text{GHz}$ and $f_c = 25.5\,\text{GHz}$, applying the time-variant channel model considering the position change of the antenna array during motion. The estimated angular power spectrum introduces an angular shift depending on the velocity.

independent of the applied transmit frequency.

Next, I investigate the behavior of the MUSIC based estimation method. The results are shown in Fig. 20 where 20(a) and 20(b) show the result for $f_c = 2.55\,\text{GHz}$ and 20(c) and 20(d) for $f_c = 25.5\,\text{GHz}$. The angular shift experienced in the conventional beamforming scenario is also present in the MUSIC estimation result. The size of the angular variation is a bit higher at lower velocity compared to the Bartlett beamformer. At higher velocity, both DOA estimation methods deliver a similar result in terms of angular variation. The possibility of overlapping components is much smaller because of the higher resolution of the subspace technique. In Section 3.3, I already showed

43

that the amplitude of the angular power spectrum changes due to the presence of the Doppler effect. The same effect can be noticed here. In addition to the results shown in the last section, the amplitude change is also dependent on the velocity caused by the movement of the antennas. Every component has a different signal strength at different velocities. This effect is stronger at mmWaves and can be better seen in Fig. 20(c) and Fig. 20(d). For an angular spectrum with a small power difference between single components as in the conducted measurement the amplitude change can be a problem. All components would be scaled differently, which could result in a completely different power spectrum. Choosing the P strongest components of the angular power spectrum can result in completely different DOA estimates.

(a) MUSIC, 20 km/h, 2.55 GHz

(b) MUSIC, 200 km/h, 2.55 GHz

(c) MUSIC, 20 km/h, 25.5 GHz

(d) MUSIC, 200 km/h, 25.5 GHz

Figure 20: MUSIC result at $f_c = 2.55\,\mathrm{GHz}$ and $f_c = 25.5\,\mathrm{GHz}$, applying the time-variant channel model considering the position change of the antenna array during motion. The estimated angular power spectrum introduces an angular shift and amplitude variation depending on the velocity and the DOA.

3.5 Further Simulation Results

In this chapter I analyze the proposed simulation scenario of Section 3.4 in terms of angular mean error as introduced in Section 2.5.3. To further evaluate the influence of the antenna movement on the implemented simulation, I vary the symbol length in Section 3.5.2.

3.5.1 Angular Mean Error

To mathematically visualize how large the error of the conducted DOA estimation methods are, I employ the metric of the angular mean calculated by Eq. 32, which is already presented in Section 2.5.3. One advantage of simulation compared to measurements is that the several parameters can be varied very easily in a reasonable amount of time. For the simulation, I vary the movement speed of the receiving antenna array from standstill up to $200\,\mathrm{km/h}$. I perform simulations with 1000 random realizations to evaluate the mean error performance of the given simulation scenario. For each realization, I choose $P = 3$ different randomly generated DOAs. All three incoming waves have the same signal strength. I apply the channel model of Section 3.4 given by (41), which takes the Doppler effect and the antenna movement into account.

The error function depending on the velocity for either of the DOA estimation methods is shown in Fig. 21. Figure 21(a) shows the result at a center frequency of $f_c = 2.55\,\mathrm{GHz}$ and Fig. 21(b) at a center frequency of $f_c = 25.5\,\mathrm{GHz}$.

First, I will go into detail about the simulation scenario at $2.55\,\mathrm{GHz}$. The mean angular error increases with growing velocity for each of the two algorithms. The MUSIC algorithm produces a higher error in terms of angular mean as the Bartlett beamformer for each of the tested velocities. The error difference between the algorithms is approximately constant during the whole simulation range. On average, the MUSIC algorithm delivers a 3% higher error in terms of angular mean than the Bartlett beamformer. At low velocity, the Bartlett beamformer performs well, with an error of only $\approx 1.1\%$ at $20\,\mathrm{km/h}$. The error is increasing fast, reaching an angular error of $19°$ at the end of the simulation range, which corresponds to a mean angular shift of $\approx 10\%$. A further increase of the velocity would only lead to a small increase of angular error. The error of the estimation applying the MUSIC algorithm starts at $\approx 4\%$ and ends at up to $\approx 11.5\%$.

On the other hand, the results slightly change for a higher center frequency of $f_c = 25.5\,\mathrm{GHz}$. At low velocities, both algorithms perform better as in the lower frequency scenario, where conducting the MUSIC algorithm generates an error of $\approx 4.5° \stackrel{\wedge}{=} 2.5\%$ and the Bartlett beamformer generate a lower mean angular error of $\approx 1° \stackrel{\wedge}{=} 0.5\%$.
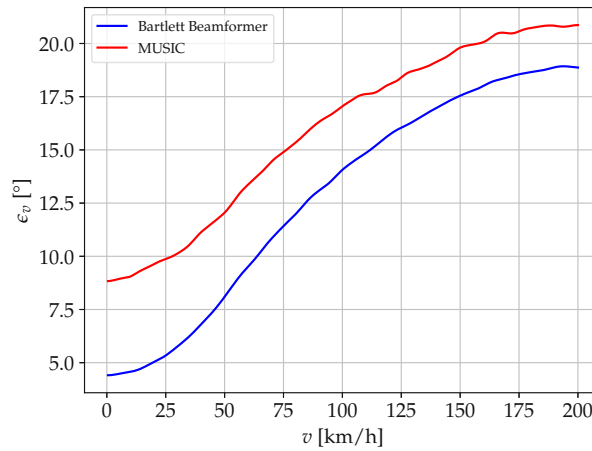
(a) Bartlett Beamformer and MUSIC, $f_c = 2.55\,\mathrm{GHz}$
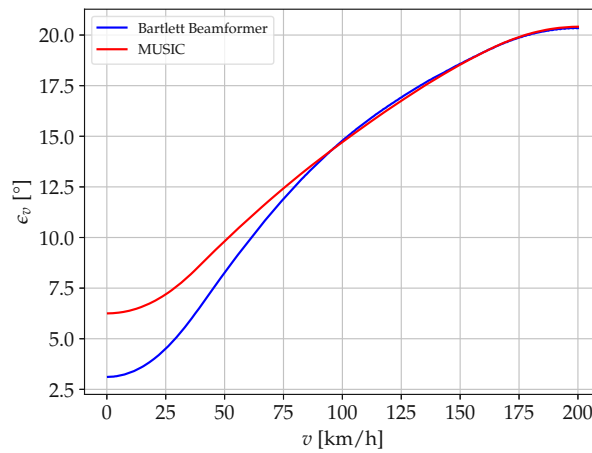
(b) [Bartlett Beamformer and MUSIC, $f_c = 25.5\,\mathrm{GHz}$

Figure 21: Mean angular error for both estimation methods at the two chosen frequencies. At the lower frequency the MUSIC algorithm performs worse than the Bartlett beamformer. In the higher frequency domain the MUSIC algorithm performs worse for lower velocities but ends with the same large error at higher velocities.

The error in the Bartlett beamforming scenario is increasing faster at a higher frequency reaching the same error as in the MUSIC scenario. Both algorithms generate an error of $\approx 21° \triangleq 11.5\%$ at a velocity of $200\,\mathrm{km/h}$. As in the lower frequency scenario, a further increase in velocity only changes the angular error slightly.

Concluding the results of the angular error, the Bartlett beamforming algorithm

performs well at lower frequencies at both frequencies. With increasing velocities it performs slightly better at a lower frequency. Conducting the MUSIC algorithm for DOA estimation leads to a worse result. At lower velocities it performs better at higher frequency and at higher velocities it delivers the same results at both frequencies.

3.5.2   Influence of the Symbol Duration

In Section 3.4, I already showed that the movement of the antennas drastically change the angular power spectrum introducing a circular shift. To investigate whether the error comes from the spare position change of the antenna array or if it depends on the traveled distance, I calculate the mean angular error by varying the symbol duration. I lower the symbol duration down to a $^1/_{100}$ of the symbol duration chosen in the previous sections.

The mean angular error with different symbol duration conducting the Bartlett beamformer for DOA estimation is shown in Fig. 22. Figure 22(a) and Fig. 22(b) depict the results at different frequencies. It is shown that with a decreasing symbol duration, the mean angular error is reduced. Using only half a symbol duration leads to an improvement of approximately $\approx 6°$, which corresponds to $\approx 3.3^{\%}$ in terms of the angular mean. A further decrease of the symbol duration also reduces the angular error. This error reduction gets smaller with decreasing symbol rate. At a frequency of $2.55\,\mathrm{GHz}$ and a symbol duration of one-hundredth of the initial symbol duration, the Bartlett Beamformer delivers a neglectable angular error, which leads to a perfect recovery of the DOAs. Note that the symbol duration cannot be reduced infinitely in real world scenarios. For the mmWave scenario the reduction of the symbol duration has the same effect. However, at a very low symbol duration, the angular error varies depending on the velocity. These variations are less than one percent.

The same results are shown in Fig. 23, applying the MUSIC algorithm for estimation. Here, Fig. 22(a) shows the angular error at a center frequency of $2.55\,\mathrm{GHz}$ and Fig. 22(b) shows the same result at a frequency of $25.5\,\mathrm{GHz}$. In the scenario with the lower frequency, we see a similar behavior as in the Bartlett beamformer estimation. The mean angular error is smaller at a lower symbol duration. Lowering the symbol duration slowly (up to one tenth of the initial symbol duration) in the mmWave scenario, it seems that all curves have a similar error of $\approx 6°$ at low velocity. By choosing only half of the symbol duration, the error is even larger than in the initial scenario for velocities smaller than $20\,\mathrm{km/h}$. With increasing speed the error in all cases is again monotonically increasing. This does not apply for a very small symbol duration. By taking only a hundredth of the symbol duration, the error is decreasing with slight variations depending on the movement speed.

47
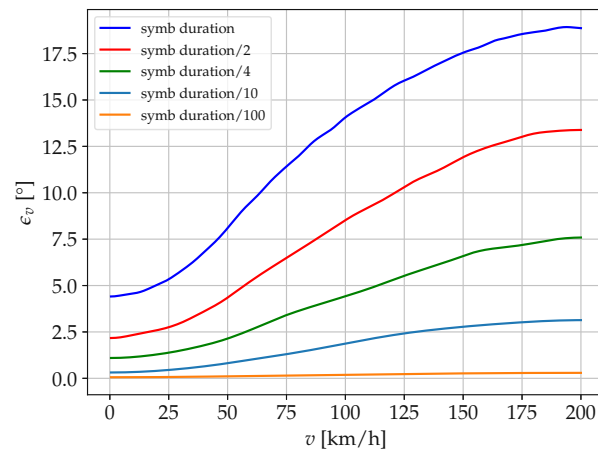
(a) Bartlett beamformer, $f_c = 2.55\,\mathrm{GHz}$
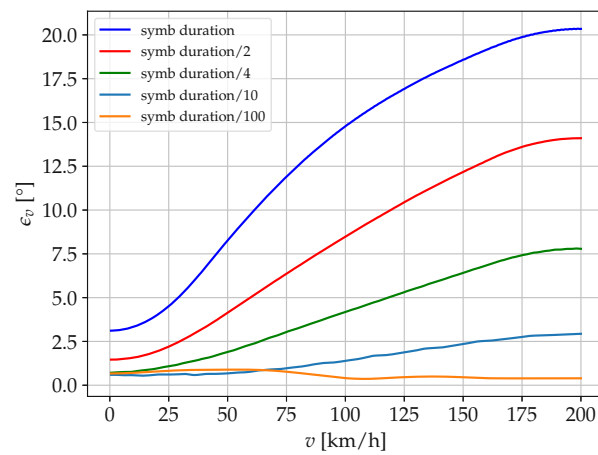
(b) Bartlett beamformer, $f_c = 25.5\,\mathrm{GHz}$

Figure 22: In this figure the error for a different symbol duration applying the Bartlett beamformer for DOA estimation. A large improvement for a smaller symbol duration can be seen.
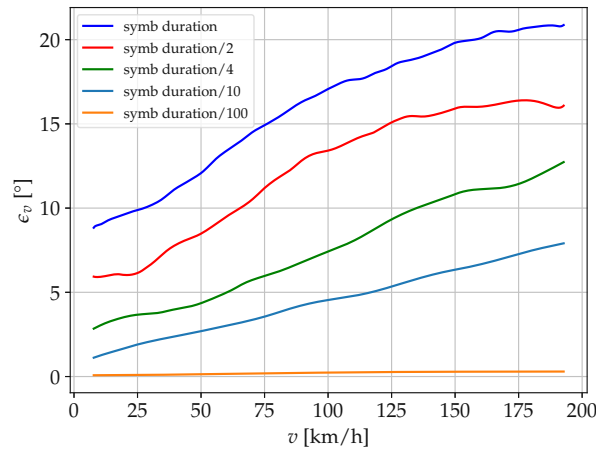
(a) MUSIC, $2.55\,\mathrm{GHz}$
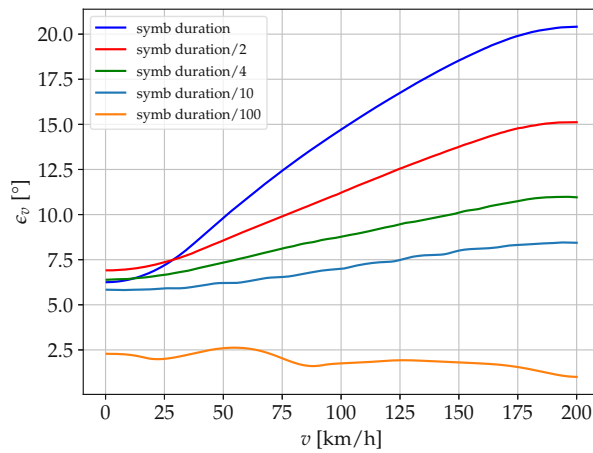
(b) MUSIC, $25.5\,\mathrm{GHz}$

Figure 23: In this figure the error for a different symbol duration applying the MUSIC algorithm for DOA estimation. Same as in the Bartlett beamformer case the angular error decreases for lower symbol duration.

3.6 Discussion and Comparison with the Measurement

The measurement shows a much higher error in terms of angular mean as the simulation in Section 3.5.1. The maximum error of the simulation is depending on the angular position of the DOA. To counteract the dependency of the angular position, I calculated the mean error performance for 1000 random realizations of the DOAs. In the measurement there is only one realization, which means that this special environment leads to a higher error in comparison with the measurement. In order to check whether the higher error only comes from the special setting, one must mimic the angular power spectrum of the measurement in the simulation. This is hard to accomplish with the proposed channel models, because the amplitude difference of the estimated angular power spectrum is small and thus, the overlays of side-lobes must be taken into account.

Next, I will compare the measurement results of Section 2.4 with the simulation results for the Bartlett beamformer estimation. I showed in Section 3.3 that the pure Doppler effect has no effect on the amplitude of the estimated angular power spectrum. The position change of the antenna analyzed in Section 3.4 not only shifts the DOAs depending on their location, it also changes the amplitude of the angular power spectrum slightly. This is caused by an overlay of DOAs or side-lobes. The relatively flat angular power spectrum of the measurement could lead to an increased variation of the amplitude change.

Now, I will focus on the comparison of the measurement results and the simulation results for the DOA estimation applying the MUSIC algorithm. In the measurement the MUSIC algorithm shows the same effect as the Bartlett beamformer. The angular power spectrum shows an angular shift and a change in amplitude. Both effects are also shown in the simulation. The Doppler effect causes an amplitude change in dependency of the angle of the DOA. That alone does not lead to a wrong DOA estimation, but it is not possible to make a concrete statement about which DOA has the strongest power. Furthermore, the movement of the antenna array leads to a cyclic shift, which is also present in the measurement results.

A reduction of the number of Symbols in the simulation in the snapshot does not influence the angular power spectrum and therefore does not change the mean angular error. Note that a minimum of $M = 144$ symbols are needed to generate a full rank sample covariance matrix. This is necessary to get a valid DOA estimation.

4   Conclusion

This thesis investigates the influence of fast movement on frequently used DOA algorithms for sub $6\,\mathrm{GHz}$ and mmWave channels. With the measuring setup proposed in Section 2, I am able to make repeatable VAA and MVAA measurements at $20\,\mathrm{km/h}$ and $200\,\mathrm{km/h}$ in the exact same indoor environment. The measurements are conducted at a center frequency of $2.55\,\mathrm{GHz}$ and also at a center frequency of $25.5\,\mathrm{GHz}$. The channel sounding procedure is further described in Section 2.3. The estimated channel data from the measurement is then used for DOA estimation. To estimate the DOA, I choose two different well-known and frequently used algorithms, the Bartlett beamformer and the MUSIC algorithm.

The results of the measurements are discussed in Section 2.5. In the standstill scenario, the MUSIC algorithm performs better than the Bartlett beamformer, because of the better spatial resolution. By adding motion to the measurement, the estimated angular power spectrum and the estimated DOAs change dramatically for both algorithms. The angular power is spread across all possible directions compared to the standstill measurements. The signal strength of the incoming waves depends on the velocity. By increasing the velocity one can also see a slight angular shift. Hardly any DOA could be reproduced in comparison with the standstill case. To get an understanding of how large the error is, I introduce the metric of the angular mean in Section 2.5.3. The error has a big range of fluctuation, going from only 3.9% up to 56%. Independent of the frequency and conducted algorithm, the error increases with rising velocity. For a center frequency of $2.55\,\mathrm{GHz}$, the Bartlett beamformer performs very poorly and produces a high error in terms of angular mean. The MUSIC algorithm works better at a lower frequency but also produces a high error at higher velocity. For a center frequency of $25.5\,\mathrm{GHz}$, the two estimation errors produce a very high error. The MUSIC algorithms is worse than the Bartlett beamformer at lower velocity than the Bartlett beamformer and has a similar performance if the velocity gets higher.

To investigate whether the Doppler shift leads to the large error in terms of the estimated angular power spectrum and following the estimated DOAs, I create a simulation scenario in Section 3. The simulation scenario should be as close to the measurement as possible. I first implement a time-invariant channel model which represents the standstill scenario. Taking the Doppler effect into account leads to a time-variant channel model. The simulation shows that the Doppler effect has no effect on the Bartlett beamformer estimation. The MUSIC algorithm also delivers the same DOA estimations as in the standstill scenario but the amplitude of the estimated angular power spectrum changes depending on the location of the DOA. Considering a Doppler frequency shift does not result in an angular shift of the angular power spectrum and both estimation methods deliver the correct angles of the DOAs.

Furthermore, I investigate the effect of a change of antenna position due to movement on the applied DOA estimation algorithms. Until now, the antenna motion during one symbol duration has been neglected because the covered distance during one symbol or snapshot is relatively small in comparison to the distance between transmitter and receiver or scattering object and receiver. This assumption is very common in real world measuring scenarios. The movement of the antenna causes an angular shift of the estimated angular power spectrum for both algorithms. The angular power spectrum generated by the Bartlett beamformer also shows a change in amplitude depending on the velocity of the antenna. For the MUSIC based estimation, the amplitude of the angular power spectrum already changes due to the presence of the Doppler effect. The same effect can be noticed here, but in addition, the amplitude of the power spectrum changes depending on the velocity. This effect is stronger for mmWaves because of the stronger Doppler shift.

As in the measurement, I calculate the mean angular error for better illustration. I vary the movement speed of the receiving antenna array from standstill up to $200\,\mathrm{km/h}$. I perform simulations with 1000 random realizations to evaluate the mean error performance of the given simulation scenario. The mean angular error increases with growing velocity for each of the two algorithms. The MUSIC algorithm produces in average a 3% higher error than the Bartlett beamformer. At a low velocity the Bartlett beamformer performs very well with an error of only 3%. At a velocity of $200\,\mathrm{km/h}$ and at a frequency of $2.55\,\mathrm{GHz}$ the error for the Bartlett beamformer is about 10% and the error of the MUSIC algorithm is 11.5%. In the mmWave Scenario the mean angular error for the MUSIC algorithm is similar, while the mean angular error gets worse for higher velocities when conducting the Bartlett beamformer. The error in the measurement is much higher than in the simulation. In the simulation, there are 1000 random realizations to evaluate the mean error while in the measurement there is only one realization. This means that the special environment could possibly lead to a higher mean angular error in comparison with the simulation.

For the simulation scenario, I also show, which influence the symbol duration has on the channel model, which takes into account the movement of the antennas. In all scenarios the reduction of the symbol duration shows an improvement in terms of the mean angular error. Using only half a symbol duration leads to an improvement of approximately $\approx 6°$, which corresponds to 3.3%. At a frequency of $2.55\,\mathrm{GHz}$ and a symbol duration of one-hundredth of the initial symbol duration, the Bartlett beamformer delivers a neglectable angular error, which leads to a perfect recovery of the DOAs. Note that the symbol duration cannot be reduced infinitely in real world scenarios. For the mmWave scenario the reduction of the symbol duration has

the same effect. However, at a very low symbol duration, the angular error varies depending on the velocity. These variations are less than one percent.

In conclusion, the movement of the antenna can influence the estimation of the DOA drastically depending on many factors. These factors include velocity, frequency, symbol length, DOA location and strength. The high error shown in the results indicate that DOA estimation algorithms, which do not consider the Doppler effect, e.g., the Bartlett beamformer or MUSIC algorithm, are not consistent anymore at fast movement.

List of Figures

List of Tables

References

[1] Sohail Payami and Fredrik Tufvesson. Channel measurements and analysis for very large array systems at 2.6 GHz. In *2012 6th European Conference on Antennas and Propagation (EUCAP)*, pages 433–437, 2012.

[2] Jakob Hoydis, Cornelis Hoek, Thorsten Wild, and Stephan ten Brink. Channel measurements for large antenna arrays. In *2012 International Symposium on Wireless Communication Systems (ISWCS)*, pages 811–815, 2012.

[3] Xiang Gao, Fredrik Tufvesson, and Ove Edfors. Massive MIMO channels — measurements and models. In *2013 Asilomar Conference on Signals, Systems and Computers*, pages 280–284, 2013.

[4] Xiang Gao, Fredrik Tufvesson, Ove Edfors, and Fredrik Rusek. Measured propagation characteristics for very-large MIMO at 2.6 GHz. In *2012 Conference Record of the Forty Sixth Asilomar Conference on Signals, Systems and Computers (ASILOMAR)*, pages 295–299, 2012.

[5] Stefan Pratschner, Sebastian Caban, Daniel Schützenhöfer, Martin Lerch, Erich Zöchmann, and Markus Rupp. A fair comparison of virtual to full antenna array measurements. In *2018 IEEE 19th International Workshop on Signal Processing Advances in Wireless Communications (SPAWC)*, pages 1–5, 2018.

[6] Binghao Chen, Zhangdui Zhong, Bo Ai, and David G. Michelson. Moving virtual array measurement scheme in high-speed railway. *IEEE Antennas and Wireless Propagation Letters*, 15:706–709, 2016.

[7] Tao Zhou, Cheng Tao, Sana Salous, and Liu Liu. Measurements and analysis of angular characteristics and spatial correlation for high-speed railway channels. *IEEE Transactions on Intelligent Transportation Systems*, 19(2):357–367, 2018.

[8] Tao Zhou, Cheng Tao, Liu Liu, Jiahui Qiu, and Rongchen Sun. High-speed railway channel measurements and characterizations: a review. *Journal of Modern Transportation*, 20(4):199–205, 2012.

[9] Xuesong Cai, Xuefeng Yin, and Antonio Perez Yuste. Direction-of-arrival estimation using single antenna in high-speed-train environments. In *2016 10th European Conference on Antennas and Propagation (EuCAP)*, pages 1–4. IEEE, 2016.

[10] Lihua Yang, Guangliang Ren, Wantao Zhai, and Zhiliang Qiu. Beamforming based receiver scheme for DVB-T2 system in high speed train environment. *IEEE Transactions on Broadcasting*, 59(1):146–154, 2013.

[11] Christoph Fischer, Hans Ludwig Blöcher, Jürgen Dickmann, and Wolfgang Menzel. Robust detection and mitigation of mutual interference in automotive radar. In *2015 16th International Radar Symposium (IRS)*, pages 143–148, 2015.

[12] Anjali Dixit, Janane Sathyamurthy, Sandeep Rao, Sanjeev Gurugopinath, and Ganesan Thiagarajan. Detection and localization of targets using millimeter wave radars: An experimental study. In *2021 IEEE International Conference on Electronics, Computing and Communication Technologies (CONECCT)*, pages 1–6, 2021.

[13] Patrick Häcker and B Yang. Single snapshot DOA estimation. *Advances in Radio Science*, 8:251–256, 2010.

[14] Sebastian Caban, Javier Rodas, and José A. García-Naya. A methodology for repeatable, off-line, closed-loop wireless communication system measurements at very high velocities of up to 560 km/h. In *2011 IEEE International Instrumentation and Measurement Technology Conference*, pages 1–5, 2011.

[15] José Rodríguez-Piñeiro, Martin Lerch, Tomás Domínguez-Bolaño, José A. García-Naya, Sebastian Caban, and Luis Castedo. Experimental assessment of 5G-candidate modulation schemes at extreme speeds. In *2016 IEEE Sensor Array and Multichannel Signal Processing Workshop (SAM)*, pages 1–5, 2016.

[16] Sebastian Caban, Ronald Nissel, Martin Lerch, and Markus Rupp. Controlled OFDM measurements at extreme velocities. In *Extreme Conference on Communication and Computing (ExtremeCom 2014)*, 2014.

[17] Faruk Pasic, Daniel Schützenhöfer, Edgar Jirousek, Robert Langwieser, Herbert Groll, Stefan Pratschner, Sebastian Caban, Stefan Schwarz, and Markus Rupp. Comparison of sub 6 GHz and mmWave wireless channel measurements at high speeds. In *2022 16th European Conference on Antennas and Propagation (EuCAP)*, pages 1–5. IEEE, 2022.

[18] David Kotz, Calvin Newport, Robert S Gray, Jason Liu, Yougu Yuan, and Chip Elliott. Experimental evaluation of wireless simulation assumptions. In *Proceedings of the 7th ACM international symposium on Modeling, analysis and simulation of wireless and mobile systems*, pages 78–82, 2004.

[19] Edward Kassem, Roman Marsalek, and Jiri Blumenstein. Frequency domain Zadoff-Chu sounding technique for USRPs. In *2018 25th International Conference on Telecommunications (ICT)*, pages 302–306, 2018.

[20] D. Chu. Polyphase codes with good periodic correlation properties (corresp.). *IEEE Transactions on Information Theory*, 18(4):531–532, 1972.

[21] Andrea Goldsmith. *Wireless Communications*. Cambridge, U.K.: Cambridge Univ. Press, 2005, 2005.

[22] H.L. Van Trees. *Optimum Array Processing: Part IV of Detection, Estimation, and Modulation Theory*. Detection, Estimation, and Modulation Theory. Wiley, 2004.

[23] Xingbin He, Zhi Zhang, and Wenjie Wang. Doa estimation with uniform rectangular array in the presence of mutual coupling. In *2016 2nd IEEE International Conference on Computer and Communications (ICCC)*, pages 1854–1859. IEEE, 2016.

[24] Shiann-Jeng Yu and Ju-Hong Lee. Design of two-dimensional rectangular array beamformers with partial adaptivity. *IEEE Transactions on Antennas and Propagation*, 45(1):157–167, 1997.

[25] Marcus Henninger, Silvio Mandelli, Maximilian Arnold, and Stephan Ten Brink. A computationally efficient 2D MUSIC approach for 5G and 6G sensing networks. In *2022 IEEE Wireless Communications and Networking Conference (WCNC)*. IEEE, apr 2022.

[26] Yi Qu, Guisheng Liao, Sheng-Qi Zhu, Xiang-Yang Liu, and Hui Jiang. Performance analysis of beamforming for MIMO radar. *Progress In Electromagnetics Research*, 84:123–134, 2008.

[27] Jeffrey L Krolik. The performance of matched-field beamformers with mediterranean vertical array data. *IEEE Transactions on Signal Processing*, 44(10):2605–2611, 1996.

[28] Hamid Krim and Mats Viberg. Two decades of array signal processing research: The parametric approach. *Signal Processing Magazine, IEEE*, 13:67 – 94, 08 1996.

[29] B.H. Fleury. First- and second-order characterization of direction dispersion and space selectivity in the radio channel. *IEEE Transactions on Information Theory*, 46(6):2027–2044, 2000.

[30] Andreas Molisch and Andreas F. Molisch. Wireless communications, 2005.

[31] Tao Zhou, Cheng Tao, and Liu Liu. Lte-assisted multi-link MIMO channel characterization for high-speed train communication systems. *IEEE Transactions on Vehicular Technology*, 68(3):2044–2051, 2018.

[32] Tao Zhou, Cheng Tao, Sana Salous, and Liu Liu. Spatial characterization for high-speed railway channels based on moving virtual array measurement scheme. *IEEE Antennas and Wireless Propagation Letters*, 16:1423–1426, 2016.

[33] Lin-Li Cui, David G Michelson, and Wen-Qin Wang. Spatial channel sounding based on bistatic synthetic aperture radar principles. *Journal of Electronic Science and Technology*, 16(3):253–270, 2018.

[34] Stefan Pratschner, Thomas Blazek, Herbert Groll, Sebastian Caban, Stefan Schwarz, and Markus Rupp. Measured user correlation in outdoor-to-indoor massive MIMO scenarios. *IEEE Access*, 8:178269–178282, 2020.

[35] David Tse and Pramod Viswanath. *Fundamentals of wireless communication*. Cambridge university press, 2005.

[36] Xiaoheng Tan, Qian Qu, Dong Jiang, Li Wen, and Lu Deng. The effects of Doppler shift on DOA estimation in TDRSS and its compensation method. *International Journal of Signal Processing, Image Processing and Pattern Recognition*, 10(12):21–34, 2017.

[37] Xianpeng Wang, Liangtian Wan, Mengxing Huang, Chong Shen, Zhiguang Han, and Tong Zhu. Low-complexity channel estimation for circular and noncircular signals in virtual mimo vehicle communication systems. *IEEE Transactions on Vehicular Technology*, 69(4):3916–3928, 2020.

[38] Rui Zhang, Feng Yan, Lianfeng Shen, and Yi Wu. A vehicle positioning method based on joint TOA and DOA estimation with V2R communications. In *2017 IEEE 85th Vehicular Technology Conference (VTC Spring)*, pages 1–5, 2017.